Winter dissolved and particulate zinc in the Indian Sector of the Southern Ocean: Distribution and relation to major nutrients (GEOTRACES GIpr07 transect)

R. Cloete[a*], J.C. Loock[a], N.R. van Horsten[a,b,c], J-L. Menzel Barraqueta[a,d], S. Fietz[a], T.N. Mtshali[e], H. Planquette[c], M.I. García-Ibáñez[f], A.N. Roychoudhury[a]

[a]Centre for Trace Metal and Experimental Biogeochemistry (TracEx), Department of Earth Sciences, Stellenbosch University, Stellenbosch 7600, South Africa.

[b]Southern Ocean Carbon and Climate Observatory, Natural Resources and Environment, CSIR, Stellenbosch, 7600, South Africa.

[c]CNRS, Univ. Brest, IRD, Ifremer, Laboratoire des Sciences de l'environnement marin, Technopôle Brest-Iroise, Plouzané, France.

[d]European Ecological Consulting S.L. (EECO), Amorebieta 48340, Spain.

[e]Department of Environment, Forestry and Fisheries, Oceans and Coast, Foretrust Building, Martin Hammerschlag Way, Cape Town, South Africa, 8001.

[f]School of Environmental Sciences, University of East Anglia, Norwich Research Park, Norwich, NR4 7TJ.

[*]Author for Correspondence: 15994619@sun.ac.za

Abstract

First winter measurements of dissolved zinc (dZn) and particulate zinc (pZn) are presented from seven stations, between 41 and 58°S, occupied in July 2017 along the 30°E longitude in the Indian Sector of the Southern Ocean. This unique spatial and seasonal dataset provided the opportunity to investigate Zn biogeochemical cycling in a region which is extremely data scarce and during a period when conditions are unfavourable for phytoplankton growth. Surface comparisons of our winter dZn and pZn to previous measurements during spring and summer revealed that Zn seasonality is most pronounced at the higher latitudes where higher dZn (and higher ratios of dZn to phosphate; dZn:PO4) and lower pZn in winter reflect decreased biological uptake and preferential dZn resupply (relative to PO4) to surface waters through deep winter mixing. The composition of pZn was majorly biogenic however localised lithogenic inputs were attributed to potential hydrothermal activity and transport of continental sediment via Agulhas waters. Calculated vertical attenuation factors (b values) for pZn (0.31) and phosphorus (P; 0.41) suggest that Zn has a longer remineralisation length scale than P, providing a mechanism as to why dZn appears to be remineralised deeper in the water column than PO4. Ratios of pZn to P (pZn:P) in surface waters increased with latitude from 1.12 to 8.28 mmol mol^{-1} due to increased dZn availability and the dominance of diatoms (with high cellular Zn quotas) in the high latitude Antarctic Zone (AAZ). Interestingly, the high surface pZn:P ratios in the AAZ did not change significantly with depth (in contrast to the northern stations where pZn:P increased with depth) suggesting the export of diatom cells below the winter mixed layer where remineralisation and rigorous mixing may resolve the linear dZn to silicic acid (dZn:$Si(OH)_4$) correlation

(dZn (nmol kg^{-1}) = 0.064 $Si(OH)_4$ (μmol kg^{-1}) + 0.690; r^2 = 0.93; n = 120) despite these elements being located in separate components of the diatom cell. Additionally, elevated concentrations of dZn and $Si(OH)_4$ below 3000 m in the AAZ may reflect nutrient accumulation in bottom waters where northward flow is inhibited by the Indian mid-Ocean ridge.

1. Introduction

Zinc (Zn) is an essential trace metal micronutrient for marine phytoplankton and its availability in the surface ocean has potential implications for biological productivity which, in turn, influences the biogeochemistry of non-metals such as carbon and nitrogen (Morel et al., 1991; Morel and Price, 2003). While Zn is a critical component in numerous enzymes involved in metabolism, perhaps the most important are the metalloproteins carbonic anhydrase and alkaline phosphatase, which enable efficient carbon fixation and the uptake of dissolved organic phosphorous, respectively (Shaked et al., 2006; Twining and Baines, 2013). However, high concentrations of dissolved Zn (dZn; > 10 nmol kg^{-1}), which can be found in estuarine and coastal upwelling settings, are known to be toxic to some phytoplankton (Sunda and Huntsman, 1996). On the other hand, low dZn concentrations (< 0.01 nmol kg^{-1}), typical of localised oligotrophic settings, could be potentially bio-limiting (Brand et al., 1983).

Owing to an increase in reliable data in the last few decades, and particularly since the onset of the GEOTRACES era (Anderson, 2020), our understanding of the processes controlling the exchange between dissolved and particulate trace metal phases are better constrained. In the surface ocean, assimilation of dZn by phytoplankton is the primary process resulting in the exchange between inorganic dZn (< 0.2 μm pore size filtered seawater) and organic particulate Zn (pZn; > 0.45 μm pore size filter) phases. Subsequent processes, e.g., zooplankton grazing, result in the formation of larger particles which either sink and contribute to the vertical export of pZn, or disaggregate (via remineralisation, desorption and dissolution) back to smaller particles contributing a source of dZn to the surface ocean (Lam and Marchal, 2015). In addition, scavenging (or adsorption) of dZn onto organic particle surfaces, and the resulting formation of larger and more rapidly sinking particulates phase, may enhance export of Zn to deeper waters (John and Conway, 2014). Similarly, authigenic Zn sulphide precipitation has been suggested in low oxygen environments with implications for pZn export in localised regions (Conway and John, 2015; Janssen and Cullen, 2015). As a result of the interplay between uptake and regeneration processes, an increase in the dZn pool typically leads to a decrease in the pZn pool. However, the exchange between dissolved and particulate phases is not necessarily proportional considering that biological and physical processes lead to differences in their residence times, i.e., years to thousands of years for dissolved phases compared with days to months for particulate phases (Lam and Marchal, 2015).

Comparing the distribution of Zn to those of the major nutrients, silicic acid ($Si(OH)_4$) and phosphate (PO_4), has proven a useful tool in constraining processes governing Zn distribution. For example, there is a tight correlation between global dZn and $Si(OH)_4$ distributions with water column concentrations of both species characterised by surface depletion and enrichments at depth (Bruland, 1980; Ellwood, 2008; Janssen et al.,

2020; Middag et al., 2019; Wyatt et al., 2014; Zhao et al., 2014). The depths at which dZn and $Si(OH)_4$ reach their greatest enrichment are deeper compared to the intermediate depth maxima displayed by global PO_4 distributions (Bruland, 1980; Middag et al., 2018; Quay et al., 2015). The relationship between dZn, $Si(OH)_4$ and PO_4 appears at odds considering that Zn and organic phosphorous (P) are associated with the organic matter of phytoplankton cells (Twining et al., 2004, Twining et al., 2003), while a negligible amount of Zn is incorporated into the siliceous frustules of diatoms (Ellwood and Hunter, 2000). It would therefore be expected that dZn, like PO_4, is regenerated at shallower depths from the rapidly dissolvable organic material and that there is no direct mechanism linking dZn and $Si(OH)_4$. Recently, two hypotheses have sought to explain this phenomenon. The first suggests that the coupling of dZn and $Si(OH)_4$ is a consequence of the natural interaction between ocean biogeochemistry and physical circulation through the Southern Ocean hub (Vance et al., 2017). In sum, Antarctic Surface Waters (AASW) are preferentially stripped of dZn and $Si(OH)_4$ relative to PO_4, consistent with the known uptake stoichiometry of diatoms in this region. Physical circulation dictates that the dZn and $Si(OH)_4$ depleted surface waters are transported to the low latitude thermocline thereby setting the low dZn, low $Si(OH)_4$ biogeochemical signature throughout much of the upper ocean (Sarmiento et al., 2004). Furthermore, the export of diatom cells beneath the winter mixed layer traps the majority of dZn and $Si(OH)_4$ in the deep ocean despite variances in their regeneration length scales. The second hypothesis adopts a more mechanistic approach whereby a secondary, deeper dZn source is inferred. The reversible scavenging model suggests that dZn is released at shallow depths from decomposing organic particles at the same rate as PO_4, however dZn is then reversibly scavenged (adsorbed) onto sinking organic particles resulting in its enhanced flux, relative to non-scavenged elements like PO_4, to the deep ocean (John and Conway, 2014; Weber et al., 2018).

Another aspect of Zn cycling requiring attention relates to seasonality. To date, the vast majority of Zn data represent spring/summer seasons, when conditions are favourable for phytoplankton growth (e.g., increased light levels, shallow mixed layers). However, little is known about Zn cycling during winter months with only two studies reporting winter Zn data for the Atlantic (Cloete et al., 2019) and Pacific (Ellwood, 2008) Sectors of the Southern Ocean. Of particular interest is winter deep mixing, a seasonally constrained physical supply mechanism whereby deeper mixing in winter compared to summer may tap into nutrient rich subsurface water masses found below the summer stratified layer. Resupply of nutrients through deep winter mixing may be critical in initiating and sustaining phytoplankton growth over the subsequent spring and summer seasons, as shown previously for iron (Tagliabue et al., 2014). Furthermore, Subantarctic Mode Water (SAMW), formed in the deep winter mixed layers of the Subantarctic Zone, is the primary communication channel between the Southern Ocean and the global low latitude upper ocean (Broecker, 1991). Therefore, investigating Zn cycling in the source region for SAMW may have important and far reaching implications as shown previously for Zn (Vance et al., 2017), $Si(OH)_4$ (Sarmiento et al., 2004) and cadmium (Middag et al., 2018; Xie et al., 2015). This study aims to address these knowledge gaps by contributing the first winter measurements of dZn and pZn from the Indian Sector of the Southern Ocean (WOCE meridional section IO6S; GEOTRACES section GIpr07).

2. Methods

2.1. Sample collection

Seawater samples were collected on-board the SA Agulhas II polar research vessel during the 2017 Winter Cruise (28/06/2017–13/07/2017). The transect followed the World Ocean Circulation Experiment (WOCE) I06S transect along the 30°E meridian in the Indian Sector of the Southern Ocean (Fig. 1A). Of the nine planned stations, seven, consisting of four deep (< 4500 m) and three shallow stations (> 1500 m), were sampled between 41°00′S and 58°30′S allowing observations to be investigated over important frontal systems and in different water masses. Two stations (IO03 and IO09) were cancelled for trace metal sampling due to intense storms present at the time of station occupation.

A vertical profile sampling method, using 24 internally Teflon-coated polyvinyl chloride (PVC) 12 L GO-FLO sampling bottles (General Oceanics), was employed at all sampling stations. GO-FLO bottles were mounted on a GEOTRACES compliant rosette frame (Cutter et al., 2017) housing a Seabird 9+ CTD (conductivity, temperature and depth) recorder. A Kevlar hydrowire with internal signal cables allowed for the transfer of data between the CTD and the on-board control room. The GO-FLO bottles were triggered at pre-determined depths during the up cast. Directly upon recovery of the rosette, the GO-FLO bottles were covered in a PVC plastic wrap in addition to their ends being covered in PVC shower caps, and were transported into a class 100 clean lab for sub-sampling. Samples for dissolved trace metal determination were collected in 125 mL acid-cleaned low density polyethylene (LDPE, Nalgene) bottles after online filtration through 0.2 µm Sartobran filters and under slight nitrogen (N_2, 99.9999% purity, BIP technology) overpressure. Samples were acidified (pH = 1.7) on-board under a laminar flow hood using hydrochloric acid (Ultrapur® HCl, Merck) and stored for later analysis. Thereafter, previously cleaned filters (25 mm diameter, Supor, 0.45 µm pore size) were mounted on acid-washed Swinnex (Millipore) filter holders which were then attached to the GO-FLO spigots and used for filtration (recorded between 5 and 10 L) of samples for particulate trace metal determination (Planquette and Sherrell, 2012). After filtration, filter holders were removed and disassembled before the sampled filter was transferred to an acid-washed polystyrene Petri-dish using clean plastic forceps. Sampled filters were subsequently frozen at −20 °C for transport back to land. All handling of filters, filter holders and samples was done under a laminar flow hood.

2.2. Dissolved zinc (dZn) determination

2.2.1. sea*FAST* and ICP-MS

Seawater samples were first preconcentrated offline by Solid Phase Extraction (SPE) on a seaFAST SC-4 DX module (Jackson et al., 2018; Rapp et al., 2017) prior to quantification by ICP-MS (Agilent 7900). During preconcentration, 10 mL of seawater was buffered to a pH of 6.0 ± 0.2 with an ammonium acetate buffer. The buffered solution was then loaded onto a column containing a high affinity metal chelating resin (Nobias PA1) where the Zn ions were bound to the resin and separated from the seawater matrix elements, e.g., Sodium (Na), Magnesium (Mg) and chlorine (Cl) which passed through the column. The Zn ions were subsequently eluted from the resin column in low volumes (250 µL) resulting in a preconcentration factor

of 40. After preconcentration, the analyte was introduced into the ICP-MS using a low self-aspirating perfluoroalkoxy (PFA) nebulizer with a flow rate of 0.2 mL min^{-1}. Isotopes of 66Zn were measured using the instruments Octopole Reaction System (ORS) in helium (He) collision mode to eliminate plasma and matrix based interferences although the latter was extensively reduced by the seaFAST matrix removal system. Online internal standard addition for drift correction was not possible using the self-aspirating nebulizer. Instead, instrument drift was monitored by running a multi-element standard (MES; verified by Inorganic Ventures) every 6 samples. Where drift exceeded 5% relative to the starting concentration of the MES for a specific element, a drift correction was applied using Eq. (1)

$$2*Conc_{MES\_start}/ (Conc_{MES\_a} + Conc_{MES\_b})*Conc_{Sample} \quad \text{Eq. 1}$$

where *a* and *b* are the MES before and after each set of 6 samples.

2.2.2. Accuracy and precision

The accuracy of the dZn analyses was verified by way of comparison with GEOTRACES reference seawater and NASS-7 certified reference material (Table 1). For the GEOTRACES SAFe D2, GSC and GSP reference seawater, our dZn values were within analytical uncertainty confirming the method's accuracy over oceanographically relevant concentrations. For the NASS-7, our dZn value was in good agreement with the certified value. To monitor ICP-MS precision, internal reference seawater (0.2 μm filtered) was collected from 55°S; 28°E during our transect (Winter Indian Southern Ocean Seawater; WISOS). The WISOS internal reference seawater was placed in the analysis sequence and results compared against each other and the calibrated mean (Table 1). The calibrated mean concentration (9.67 ± 0.23 nmol kg^{-1}) was established by replicate analysis (n = 10) of the WISOS in conjunction with the SAFe and NASS-7 reference materials. The in-sequence analysis of the WISOS (n > 30) yielded a value of 9.63 ± 0.24 nmol kg^{-1} confirming the method's precision.

2.2.3. Blanks and limits of detection

The instrument (ICP-MS) blank was quantified by introducing a solution of un-preconcentrated 2% HNO_3, identical to the seaFAST eluent, in ultra-pure deionized water. The instrument blank was 0.07 ± 0.01 nmol kg^{-1} for Zn (Table 1). To determine the blank contribution from the method, a solution of HNO_3 (ultrapur®, Merck) diluted to 2% with ultra-pure deionized water, the same composition as the eluent used in sample preconcentration, was analysed. The blank was subjected to the same preconcentration procedure as the seawater samples. The method blank was 0.09 ± 0.01 nmol kg^{-1} and was subtracted from sample values. The limit of detection (LOD), calculated as three times the standard deviation of the preconcentrated blank, was 0.02 nmol kg^{-1}.

2.2.4. Data processing

Samples for dZn were analysed in duplicate. The final value represents the mean of duplicate measurements. In cases where the percentage relative standard deviation (%RSD) between the duplicate measurements was > 10% (n = 13), one of the values was deemed a suspected outlier and not used further. This was determined by curve fitting the data points based on the values above (shallower depth) and below

(deeper depth) the suspect value as well as by comparison with other parameters (salinity, temperature, and nutrients) measured from the same GO-FLO bottle.

2.3. Phosphate (PO_4) and silicic acid ($Si(OH)_4$) determination

Macronutrient concentrations were described previously (Weir et al., 2020). Here, we briefly summarise the analytical methods. Seawater samples for PO_4 and $Si(OH)_4$ analysis were collected from GO-FLO bottles, filtered immediately after collection using a 0.2 µm pore size syringe filter into 50 mL Falcon® tubes and frozen at −20 °C. Macronutrient analysis was done at the Marine Biogeochemistry Laboratory at the University of Cape Town (MBL-UCT). PO_4 was determined manually by colorimetric method (Grasshoff, 1983) with an analytical error of ±0.06 µmol kg^{-1}. $Si(OH)_4$ was analysed using a Lachat Quick-Chem flow injection analyser (Wolters, 2002) with an analytical error of ±0.2 µmol kg^{-1}.

2.4. Particulate Zn (pZn) and phosphorous (P) determination

Samples for particulate trace metals were analysed at the Université de Bretagne Occidentale (UBO). Details of the analytical procedure have been previously described (Planquette and Sherrell, 2012) and are presented briefly here. The pZn samples were processed and analysed 6 months after sample collection. Filters containing the samples were acid reflux digested at 130 °C in acid-cleaned Savillex vial. Archive solutions were stored in 3 mL of 0.12 M HNO_3 (Ultrapur® grade), of which 250 µL was diluted up to 2 mL for analysis by sector field inductively coupled plasma mass spectrometry (SF-ICP-MS, Element XR Thermo Scientific). Samples were spiked with 1 µg L^{-1} indium (In) as an internal standard to correct for instrument drift. Three certified reference materials (PACS 3, MESS 4 and BCR 414) were processed as samples and analysed for pZn and P to assess the accuracy of the methodology (Table 2). The certified reference materials yielded mean percentage recoveries of 108%, 100% and 97% for pZn, and 100%, 106% and 95% for P (PACS 3, MESS 4 and BCR 414, respectively). Filter blanks (1.51 pM and 0.08 nM for pZn and P, respectively) were determined by digesting and analysing an acid-washed filter. The detection limits, defined as three times the standard deviation of the blanks, for pZn and P were 2.82 pmol kg^{-1} and 0.03 nmol kg^{-1}, respectively (n = 5).

2.5. Estimating pZn composition

The lithogenic fraction of the total pZn (pZn_{lith}) was calculated by multiplying the particulate aluminium (pAl) concentration (Van Horsten et al., 2021) with the Zn/Al upper continental crust (UCC) ratio of 0.00163 (Rudnick and Gao, 2013). The non-lithogenic fraction (assumed to be the biogenic fraction) of the total pZn (pZn_{bio}) was then calculated by subtracting the lithogenic fraction of pZn from the total pZn (Eq. (2)). Unless otherwise stated, pZn in this manuscript refers to pZn_{bio}.

$$pZn_{bio} = [pZn] - ([pAl] \times (Zn/Al)_{UCC}) \quad \text{Eq. 2}$$

2.6. Calculation of vertical attenuation factors (*b* values)

The remineralisation length scale of an element is determined by the attenuation of the downward particle flux settling gravitationally and is element specific (Boyd et al., 2017). The attenuation of Zn with depth

was modelled using the Martin equation (Martin et al., 1987), originally developed for particulate organic carbon, modified for Zn (Eq. (3)), P and cadmium accordingly (Ellwood et al., 2020). Particulate cadmium data are from Cloete et al. (2021).

$$[pZn_z] = [pZn_{MLD}](z/MLD)^{-b} \quad \text{Eq. 3}$$

Where $[pZn_z]$ is the pZn concentration at depth z, $[pZn_{MLD}]$ is the pZn concentration nearest the base of the Mixed Layer Depth (MLD) at each station and *b* is the vertical attenuation factor. Model fits of the particulate data were optimised by minimising the square of the differences between observational data and the model output.

2.7. Extended optimum multiparameter (eOMP) analysis

An extended optimum multiparameter (eOMP) analysis (Karstensen and Tomczak, 1998) was used to solve the water mass structure of the section. Briefly, eOMP analyses consider that the observed physicochemical properties of a given water sample can be formulated as a linear combination of a finite number of water masses represented by the so-called source water types (SWTs; Tomczak, 1999). The SWTs are points in the n-dimensional parameter space, where n is the number of properties that characterize SWTs. In this work, the SWTs are characterised by potential temperature, salinity, oxygen, nitrate, PO_4 and $Si(OH)_4$ (Table 3). Once the SWTs and their physicochemical properties are defined, the goal of an eOMP analysis is to find the fractions of each SWT (Xi) in each water sample and does so by a least-square method constrained to be positive definite:

$$d = G * X_i + \Delta O_{2bio}/R + \varepsilon \quad \text{Eq. 4}$$

where d is the observed property in a water sample, G is the matrix containing the properties defining the SWTs, X_i is the relative contributions of each SWT to the sample, ΔO_{2bio} accounts for the changes in oxygen due to the synthesis and/or remineralisation of the organic matter, R are the Redfield-like stoichiometric ratios, and ε is the residual. In this study we used an R of 12 for $Si(OH)_4$ (Castro et al., 1998; Perez et al., 1993), 175 for PO_4 and 10.5 for nitrate (Anderson and Sarmiento, 1994; Takahashi et al., 1985).

The eOMP analysis was used to locate the realm of Antarctic Bottom Water (AABW), and therefore the eOMP analysis was restricted to water samples > 1000 m. For this purpose, only four SWTs were selected: Upper Circumpolar Deep Water (UCDW), Lower Circumpolar Deep Water (LCDW), North Atlantic Deep Water (NADW), and AABW. In this work, we selected the properties for UCDW from Carter et al. (2014); and those of LCDW, NADW, and AABW from Liu and Tanhua (2021). The eOMP analysis was reliable since it explained 99% of the changes in the conservative tracers (Table 3).

3. Results

3.1. Description of the study area

3.1.1. Frontal positions

The Southern Ocean is dominated by the uninterrupted, eastward flowing Antarctic Circumpolar Current (ACC). Another major current, the Agulhas current (AC) flows southward along the east coast Africa before retroflecting at the southern tip of the continent due to shear interactions with the ACC. The resulting Agulhas Return Current (ARC) flows eastward and intersects the 30°E section at ~40°S (Barrett et al., 2018). A number of important oceanographic fronts run parallel with the ACC and divide the Southern Ocean into distinct biogeochemical zones (Fig. 1A). Frontal positions were determined previously (Weir et al., 2020) following temperature, salinity and oxygen criteria (Belkin and Gordon, 1996; Orsi et al., 1995; Pollard et al., 2002). To the north of the transect, the Subtropical Front (STF) at 42.4°S separated the Subtropical Zone (STZ) to the north from the Subantarctic Zone (SAZ) to the south. Likewise, the Subantarctic Front (SAF) at 46.2°S separated the SAZ in the north from the Polar Frontal Zone (PFZ) to the south which, in turn, was bounded in the south by the Antarctic Polar front (APF) at 49.3°S. Further south, the Antarctic Zone (AAZ) extended until the Southern Boundary (SBdy) at 58.5°S, incorporating the Southern Antarctic Circumpolar Current Front (SACCF) at 56.5°S. The Marginal Ice Zone (MIZ), defined as 30% ice cover, was encountered at 61.7°S (de Jong et al., 2018), south of the southernmost sample station.

3.1.2. Water mass characterisation

Numerous water masses were sampled throughout the study (Fig. 1B; water mass definitions found in Anilkumar et al., 2006; Orsi et al., 1995). The hydrography of the Southern Ocean is largely defined by the upwelling and ventilation of deep waters at the higher latitudes. As a consequence of wind-driven forcing, nutrient-rich UCDW, identified at a potential temperature (θ) of 2.0–2.5 °C and potential density (σ_θ) of 27.2–27.8 kg m^{-3}, upwells south of the APF. Near the surface, a portion of the upwelled water moves south, as AASW ($\theta \leq 2.5$ °C), where continued cooling and sea-ice formation increase water density initiating subduction and eventual formation of cold (θ = ~0 °C; σ_θ = 27.8–27.9 kg m^{-3}) AABW, which flows northward along the basin floor (Orsi et al., 1999). In the upwelling region, the remaining portion of upwelled UCDW flows northward via Ekman drift. Here, surface waters warm rapidly toward the north forming Subantarctic Surface Water (SASW; θ = 7–12 °C) and Subtropical Surface Water (STSW; $\theta \geq 12$ °C). Subducting northward below the surface water masses were Antarctic Intermediate Water (AAIW; θ = 2.5–5.0 °C, σ_θ = 26.7–27.4 kg m^{-3}) and SAMW (θ = 12–15 °C, σ_θ = 26.2–26.6 kg m^{-3}). Intermediate and mode waters are the chief communicators between the major ocean basins exporting their biogeochemical signatures to the lower latitude oceans (Gordon et al., 1992). Deeper in the water column, NADW, identified chiefly by a deep salinity maximum (S > 34.80; van Aken et al., 2004) was generally characterised by lower concentrations of all major nutrients in relation to the overlying UCDW and underlying LCDW (θ = 1.5–2.0 °C; σ_θ = 27.8–27.9 kg m^{-3}).

3.1.3. Surface mixed layer and remineralisation depth

The Surface Mixed Layer (SML) at each station was defined as the area between the sea surface and the MLD, which was determined as the depth between 10 m and 400 m at which the Brunt Väisälä frequency (BVF) squared reach a maximum (Weir et al., 2020). Along this transect, the STZ had the shallowest MLD (122 m) while the SAZ was characterised by the deepest MLDs observed (190–220 m). Further south, the MLD generally increased from 134 m in the PFZ to 125–161 m in the AAZ. The remineralisation depth was approximated at 500 m for all stations based on the observation that at this depth, vertical profiles of P (and pZn) converged on low values (Fig. S1), representative of the deep water values.

3.2. Distribution of dissolved elements

3.2.1. dZn

At each station, dZn (Figs. 2A, S1 and S2) was lowest in surface waters and increased to local maxima in the deepest sample. The lowest measured dZn was in STSW (0.44 ± 0.28 nmol kg^{-1}) while highest concentrations were observed in AABW (8.67 ± 0.42 nmol kg^{-1}), sampled south of the Indian ridge (located broadly between 48°S and 52°S) below 3000 m depth. Surface water dZn concentrations increased southwards by approximately 8-fold between STSW in the north and AASW (3.37 ± 0.28 nmol kg^{-1}) to the south. Concentrations of dZn in AAIW was 3.67 ± 1.79 nmol kg^{-1} while dZn in UCDW was 5.89 ± 1.06 nmol kg^{-1}. In general, NADW was characterised by slightly lower dZn concentrations relative to surrounding water masses. For example, in the PFZ (St. IO05; 48°S), dZn in NADW was 4.91 ± 0.20 nmol kg^{-1}, 5.14 ± 0.89 nmol kg^{-1} in the overlying UCDW and 6.62 ± 0.03 nmol kg^{-1} in the underlying LCDW. In deep waters (> 2500 m) north of the Indian ridge (St. IO05 and IO06), dZn was 5.71 ± 1.18 nmol kg^{-1} while to the south (St. IO04 and IO02) dZn was 8.51 ± 0.37 nmol kg^{-1}.

3.2.2. PO_4 and $Si(OH)_4$

Concentrations of PO_4 and $Si(OH)_4$ (Fig. S1) have been previously reported (Weir et al., 2020) and are briefly described here. Surface (25 m) PO_4 increased southward from 0.22 to 1.78 μmol kg^{-1} while $Si(OH)_4$ increased from 2.93 to 46.8 μmol kg^{-1}. At each station PO_4 increased with depth until a mid-depth maximum (between 2.20 and 2.67 μmol kg^{-1} at 41 and 48°S, respectively) located within the southward upwelling UCDW. In contrast to PO_4, vertical profiles of $Si(OH)_4$ increased to maximum concentrations at the deepest depth sampled (like dZn) and reached a maximum concentration of 132 μmol kg^{-1} in AABW (3500 m) at 50°S.

3.3. Distribution of particulate elements

3.3.1. pZn

Depth profiles of pZn (Figs. 2B, S1 and S2) typically had highest concentrations near the surface, particularly in the AAZ where surface water pZn was 0.106 ± 0.029 nmol kg^{-1}. To the north, surface water pZn was 0.068 ± 0.009 nmol kg^{-1} in the PFZ, 0.037 ± 0.012 nmol kg^{-1} in the SAZ and 0.021 ± 0.006 nmol kg^{-1} in the STZ. There was no clear trend in intermediate and deep water pZn distributions. Below 1000 m depth, pZn was 0.033 ± 0.016 nmol kg^{-1} south of the APF and 0.022 ± 0.011 nmol kg^{-1} north of the APF.

The composition of pZn was dominated by pZn_{bio} (pZn (nmol kg^{-1}) = 0.960 pZn_{bio} (nmol kg^{-1}) + 0.004; r^2 = 0.99; n = 120). However, there were localised areas where pZn_{lith} contributed significantly to pZn (Fig. 2C). For example, below the surface layer (> 250 m) in the STZ, pZn_{lith} was 0.007 ± 0.001 nmol kg^{-1} equating to between 16 and 68% of total pZn. In the SAZ, pZn_{lith} was 0.004 ± 0.001 nmol kg^{-1} below the surface layer (10–45% of pZn). In the AAZ, pZn_{lith} was low (0.002 ± 0.001 nmol kg^{-1}) throughout the water column with the exception at the deepest sample at 50°S, above the mid-ocean ridge, where pZn_{lith} was 0.01 nmol kg^{-1} (30% of pZn).

3.3.2. P

The distribution of P (Fig. S1) was characterised by high surface concentrations, rapid decreases through subsurface water masses and low (< 2.5 nmol kg^{-1}) concentrations below 1000 m depth. Highest surface water (25 m) P concentrations were measured in the PFZ (27.5 nmol kg^{-1}) and SAZ (15.9–24.7 nmol kg^{-1}) and were lower in the AAZ (9.43–17.0 nmol kg^{-1}) and STZ (15.4 nmol kg^{-1}).

4. Discussion

4.1. Seasonal insights into Zn cycling

The data presented here contributes the first winter measurements of dZn and pZn from the 30°E longitude in the Indian Sector of the Southern Ocean. For comparative purposes, a global compilation of dZn and pZn measurements (Fig. S3) was created from available data in the GEOTRACES Intermediate Data Product (IDP) 2017 (Schlitzer et al., 2018; see figure caption for dataset references). While the compilation demonstrates the usefulness of the GEOTRACES IDP, we focus our comparison on the Southern Ocean where we compared our surface dZn (Fig. 3A) and pZn (Fig. 3B) to a compilation of measurements (including data not in the IDP) covering all three Southern Ocean Sectors and multiple seasons in order to assess seasonal variations and identify potential drivers thereof (Barrett et al., 2018; Butler et al., 2013; Cloete et al., 2019; Coale et al., 2005; Croot et al., 2011; Ellwood, 2008; Ellwood et al., 2020; Janssen et al., 2020; Löscher, 1999; Sieber et al., 2020; Wang et al., 2018). We acknowledge the limitations of such a comparison where, for example, shifts in frontal positions, changes in ambient nutrient availability and differences in the resident phytoplankton community between sample locations could potentially influence Zn distributions. Nevertheless, the comparisons do yield interesting observations regarding Zn seasonality. There is a fairly consistent latitudinal trend for surface dZn whereby concentrations were lowest north of ~46°S, increased southward until maxima in the upwelling zone, between 52°S and 56°S, and were generally lower in surface waters south of 56°S. Seasonal dZn differences were least apparent in the region north of 46°S where our winter Indian Sector dZn (0.46 ± 0.16 nmol kg^{-1}; n = 3) was comparable to winter (0.33 ± 0.16 nmol kg^{-1}; n = 3) and summer Pacific Sector data (0.34 ± 0.23 nmol kg^{-1}; n = 3). Interestingly, winter dZn in the Pacific Sector remained low (0.28 ± 0.11 nmol kg^{-1}; n = 6) between 46°S and 52°S while dZn increased significantly during our transect (and for all other datasets). The low dZn in the Pacific Sector coincided with low $Si(OH)_4$ (< 3.49 µmol kg^{-1}) which extended until the SAF at ~52°S, much further south compared to the position of the SAF during this study (~46°S), illustrating the impact of frontal positions

and nutrient availability on dZn distributions. Further south, in the upwelling zone, seasonal dZn differences were more apparent. For example, at 56°S, our winter Indian Sector dZn value (4.19 nmol kg^{-1}) was slightly higher than the spring Atlantic Sector (3.80 nmol kg^{-1}) and significantly higher compared to summer measurements in the Atlantic (2.81 nmol kg^{-1}) and Pacific (0.11 nmol kg^{-1}) Sectors. The same trend was evident for ratios of dZn to PO_4 (dZn:PO_4; Fig. S4) at 56°S whereby ratios were highest in winter (2.17 mmol mol^{-1}) and decreased in spring (2.02 mmol mol^{-1}) and summer (1.73 and 0.65 mmol mol^{-1}; Atlantic and Pacific Sectors, respectively). As a result of unfavourable growth conditions for phytoplankton during winter (e.g., lower light levels and deeper mixed layers than in spring/summer), the higher dZn (and dZn:PO_4) in winter likely reflects decreased biological uptake by diatoms as well as deep winter mixing whereby dZn is preferentially resupplied (relative to PO_4) to surface waters through access to dZn-enriched waters below the spring/summer mixed layers. The source of excess Zn in subsurface waters is predominantly a water mass characteristic reflecting preformed concentrations and non-local dZn accumulation from remineralisation throughout the ocean. In an attempt to assess the relative importance of biological uptake and deep winter mixing in driving the dZn seasonal signal, we calculated the theoretical dZn uptake (at three locations; in the SAZ, PFZ and AAZ) based on the observed PO_4 seasonal signal i.e. the difference between summer (Sieber et al., 2020) and winter (this study) concentrations averaged over the mixed layer, and the summer dZn/PO_4 uptake ratio (calculated from the slope of regression between dZn and PO_4 in the winter mixed layer). We then compared the theoretical dZn uptake value to the measured dZn seasonal signal (as calculated for PO_4) assuming the difference to reflect additional dZn supply from a combination of deep winter mixing, lateral advection or remnants from the previous growth season. We calculate an expected dZn uptake of 0.22, 0.24 and 0.57 nmol kg^{-1} in the SAZ, PFZ and AAZ respectively (Table S1), compared to measured winter-summer dZn differences of 0.79, 0.58 and 0.87 nmol kg^{-1}. Ultimately results suggest that, at high latitudes (AAZ), differences in biological uptake predominantly drive the seasonal dZn signal while at lower latitudes (PFZ and SAZ), deep winter mixing, lateral advection and remnant dZn signatures become progressively more important.

For pZn (Fig. 3B), comparable data was more scarce than for dZn. North of 50°S, our winter surface pZn (0.05 ± 0.04 nmol kg^{-1}) was comparable to corresponding summer measurements (0.09 ± 0.02 nmol kg^{-1}; n = 2). Between 50°S and 58°S (the southern extent of our transect) our winter pZn remained low, below 0.12 nmol kg^{-1}, while summer pZn increased to 0.28 ± 0.12 nmol kg^{-1} reflecting the increased uptake of Zn under favourable growth conditions. South of 58°S, summer pZn remained high (0.48 ± 0.22 nmol kg^{-1}; n = 7) while spring pZn was lower (0.21 ± 0.12 nmol kg^{-1}; n = 5) yet still higher than winter pZn slightly to the north. A southward increasing trend was also evident in ratios of pZn to P (pZn:P; Fig. S4) although the magnitude of the pZn:P increase varied between seasons as well as location suggesting Zn uptake is not fixed to that of P.

4.2. Factors controlling Zn uptake in surface waters

The phytoplankton community present during this transect was active with winter biomass accumulating to levels similar to the lower end of comparable summer measurements (Weir et al., 2020). The uptake of Zn by phytoplankton in surface waters is related primarily to the availability of Zn (Middag et al., 2019; Morel et al., 1994; Sunda and Huntsman, 1995) but may also be influenced by the availability of other metals such as iron (Fe). Interestingly, both increases (Twining et al., 2004) and decreases (Cullen et al., 2003) in the pZn:P ratio of resident phytoplankton communities have been observed following Fe addition, suggesting varied cellular responses to Fe-stimulated growth. In an effort to investigate the drivers of Zn uptake during this study, we compare dZn, pZn and pZn:P averaged over the SML (Fig. 4). In addition, $Si(OH)_4$ and dissolved Fe (dFe; see Table S2 for data validation) are also shown. There was a strong southward increase in dZn concentrations, which increased from 0.20 nmol kg^{-1} in the STZ to a maximum of 3.66 nmol kg^{-1} in the AAZ, driven by upwelling of deep waters enriched in Zn and other nutrients, e.g., $Si(OH)_4$ (Vance et al., 2017). Similarly, P and pZn:P ratios increased southward. For example, pZn:P increased from 0.97 mmol mol^{-1} in the STZ to a maximum of 8.58 mmol mol^{-1} in the AAZ. In contrast, dFe concentrations were > 1 nmol kg^{-1} north of the APF and were lowest in the AAZ (0.04 ± 0.01 nmol kg^{-1}).

The clear association between dZn and pZn with latitude suggests Zn availability is the primary driver of Zn uptake. However it must be noted that Zn uptake rates are related to the free Zn concentration rather than the total Zn concentration (Baars and Croot, 2011; Brand et al., 1983; Saito and Goepfert, 2008). Organic complexation may potentially reduce biological uptake in surface waters of the STZ and SAZ where dZn is low and the concentration of Zn-binding ligands may saturate dZn (Baars and Croot, 2011). In the PFZ and AAZ however, the high surface dZn saturates ligand concentrations equating to high bioavailable dZn. Our pZn:P ratios (7.68 ± 1.14 mmol mol^{-1}) from the diatom dominated AAZ (Fig. S5) were higher compared to previous measurements along this transect (3.00 ± 0.90 mmol mol^{-1}; Barrett et al., 2018), where a more diverse phytoplankton assemblage was likely present, and compared more similarly to diatom dominated assemblages from elsewhere in the Southern Ocean (8.10–14.90 mmol mol^{-1}; Barrett et al., 2018; Cullen et al., 2003; Twining et al., 2004). Diatoms require $Si(OH)_4$ to build their siliceous frustules and the high $Si(OH)_4$ in the AAZ (26–48 μmol kg^{-1}), compared to the northern zones (2–5 μmol kg^{-1}), allowed diatoms to dominate the phytoplankton community assemblage. While $Si(OH)_4$ was highest in the AAZ, dFe was lowest and likely limited diatom growth. There is evidence that suggests cellular pZn:P ratios are influenced by Fe availability and our data indicate higher pZn:P under low Fe conditions, possibly via reduced growth rates and accumulation of Zn (and other metals) relative to organic biomass (Cullen et al., 2003). The low $Si(OH)_4$ in surface waters close to and north of the APF allowed flagellates to out compete diatoms (Weir et al., 2020). The pZn:P of flagellates in the Southern Ocean does show latitudinal variation likely linked to Zn availability (i.e., higher pZn:P in the high dZn waters south of the APF) however, the pZn:P of flagellates was at least four times less than co-occurring diatoms

(Twining and Baines, 2013) suggesting flagellates have lower P normalised Zn quotas and providing further reasoning behind the low pZn:P at the northern stations. Therefore, in addition to the primary control exerted by Zn availability, the availability of dFe and changes in phytoplankton taxonomy may influence pZn:P ratios in surface waters.

4.3. Differences in remineralisation length scales between zinc, phosphorus and cadmium

Vertical attenuation factors (*b* values) for pZn, P and particulate cadmium (pCd) were calculated for full depth profiles and to 1000 m (Table 4) in order to investigate the relative remineralisation length scales for these elements. For the full depth profiles, *b* values were slightly higher than for < 1000 m with the exception of pZn at 41°S and 43°S where the exclusion of high pZn concentrations (0.042 and 0.048 nmol kg^{-1}, respectively) measured at 1500 m caused increased *b* values. For simplicity, we focus on *b* values for the full dataset. For pZn, a *b* value of 0.33 was obtained however there was significant latitudinal variation between zones with lower values in the STZ and SAZ (0.18–0.24) and higher values in the PFZ and AAZ (0.27–0.50). Importantly, at all stations the *b* value for pZn was lower than that of P and pCd. Overall, our *b* values for pZn, P (0.41) and pCd (0.46) suggest a longer (slower) remineralisation length scale for pZn compared to P and pCd, in agreement with the sequence of Ellwood et al. (2020). Scaled to P, our *b* value for pZn is higher compared to Ellwood et al. (2020) and compares more similarly to Boyd et al. (2017). The differences in remineralisation length scales for these elements are likely related to their specific physiological association within the cell. For example, Zn is a constituent of a host of metalloproteins (Zn-finger proteins) such as carbonic anhydrase, alkaline phosphatase, and RNA polymerase (Twining and Baines, 2013) whereas P is located in ATP, DNA, RNA and phospholipid membranes (Raven, 2013 and references therein) ultimately leading to differences in lability between Zn and P. As remineralisation reflects the release of these elements from sinking organic matter (i.e., from particulate to dissolved phase), longer length scales translate to a deeper release and should be reflected in the depth profiles of pZn to P (pZn:P) and dZn to major nutrients (dZn:PO_4 and dZn:$Si(OH)_4$).

4.3.1 pZn:P

Depth profiles of pZn:P generally showed increases with depth, particularly in the upper water column (Fig. 5). The increase was most pronounced in the STZ (Fig. 5A) where pZn:P was low at the surface (0.89 mmol mol^{-1}) and increased more than 5-fold by 500 m. This factor was between 4 and 5 in the SAZ (Fig. 5B–C), 3 in the PFZ (Fig. 5D) and approximately 1 throughout the AAZ (Fig. 5E–G) indicating progressively weaker gradients toward the south. Previously, pZn:P ratios from the Southern Ocean Time Series (SOTS), located in the SAZ, showed a pZn:P depth increase of approximately 4-fold (Ellwood et al., 2020), in agreement with our SAZ data. The trend of increasing pZn:P ratios with depth is consistent with the lower b value (longer remineralisation length scale) for Zn than P and is clearly illustrated when comparing the decreases in pZn and P (as a percentage of their respective maximum) with depth (Fig. 5). The pZn and P maxima were generally at the same (or very similar) depths. However, below the concentration maximum,

P decreased more rapidly than pZn (by 500 m, P decreased to values between 9 and 26% of the P maximum whereas pZn decreased to values between 20 and 59% of the pZn maximum). In the AAZ, pZn:P ratios did not increase significantly with depth, suggesting more similar remineralisation length scales for these two elements in this region. This is consistent with P-normalised b values (Table 4) in the AAZ which were closer to 1 (0.76–0.97) than at the stations north of the APF (0.33–0.61). The weaker pZn:P depth gradient was the result of high ratios at the surface, likely driven by diatoms with elevated pZn:P cellular stoichiometries. Our results are similar to previous observations showing no significant changes in pZn:P ratios with depth from a diatom dominated phytoplankton assemblage (Twining et al., 2014) and highlight the possible taxonomic effect on Zn cycling. Reversible scavenging has also been suggested to play an important role in Zn cycling (John and Conway, 2014). The increase in pZn:P with depth at the northern stations potentially indicates a role for reversible scavenging in influencing Zn cycling whereby pZn is remineralised at the same rate as P but is then rapidly adsorbed onto organic particles resulting in an apparent deeper regeneration than P (Weber et al., 2018). However, pZn:P does not show significant increases with depth in the AAZ, where we would expect the strongest scavenging signal as there is more Zn available. Our data therefore suggests that scavenging might be a less important component of Zn cycling at the higher latitudes.

4.3.2 dZn:PO_4 and dZn:$Si(OH)_4$

Differences in the remineralisation length scales of Zn and P were observed in the dissolved phase data as well. A plot of dZn vs PO_4 shows a curvilinear relationship whereby the change in dZn concentration relative to PO_4 ($\Delta dZn/\Delta PO_4$) increases with depth (Fig. 6A) reflecting the deeper release of dZn compared to PO_4 from sinking organic matter. In contrast to dZn:PO_4, a plot of dZn vs $Si(OH)_4$ showed a strong linear relationship (Fig. 6B; dZn (nmol kg^{-1}) = 0.064 $Si(OH)_4$ (μmol kg^{-1}) + 0.690; r^2 = 0.93; n = 120), a well-documented feature in the Southern Ocean and most of the global ocean (De Souza et al., 2018 and references therein). The linear correlation suggests a similar remineralisation length scale for Zn and $Si(OH)_4$. Calculated *b* values for biogenic silica (bSi; 0.22 ± 0.53; Boyd et al., 2017) span the range of our *b* values for P (0.41) and pZn (0.33) preventing meaningful comparison. However, considering the observed decoupling between vertical profiles of dZn and PO_4, and close coupling of dZn and $Si(OH)_4$, we would expect the *b* value for bSi to be more similar to that of pZn than P. Ultimately, diatoms in the high latitude Southern Ocean play a significant role in Zn cycling as a result of their unique uptake stoichiometries. However, it is unlikely that this mechanistic link alone can explain the global trends observed for Zn-PO_4 and Zn-$Si(OH)_4$.

4.4. Upwelling and lateral transport of Zn signatures

In addition to a taxonomic role, the physical water mass circulation pattern in the Southern Ocean is a critical component of Zn and major nutrient cycling owing to the transport of biogeochemical signatures, set in the high latitude AAZ, throughout much of the global low latitude ocean (Vance et al., 2017). To elaborate, the net result of biological uptake by diatoms in the AAZ are surface waters that are depleted in

dZn and $Si(OH)_4$ with respect to PO_4. Physical circulation dictates that the resulting dZn and $Si(OH)_4$ deficient surface waters are transported northward across the APF. Furthermore, a portion of the northward flowing surface water subducts in the PFZ and SAZ, forming SAMW with inherently low dZn and $Si(OH)_4$ concentrations relative to PO_4. Considering that SAMW is the main communication channel to the global low latitude thermocline (Sarmiento et al., 2004), the northward transport of SAMW provides a likely mechanism for the observed dZn and $Si(OH)_4$ depleted waters of the low latitude upper ocean. One of the key components of the Vance et al. (2017) hypothesis is the export of diatom cells below the winter mixed layer thus setting the deep Southern Ocean Zn-P and Zn-$Si(OH)_4$ relationships. Our pZn:P data from the AAZ shows high ratios below the winter mixed layer, indicating export of diatom cells to the subsurface, where remineralisation and vigorous mixing may resolve the deep water dZn-$Si(OH)_4$ correlation despite being located in separate components of the diatom cell (Vance et al., 2017).

4.5. Sources of pZn_{lith}

The low pZn_{lith} (~0.001 nmol kg^{-1}) throughout the SML of the AAZ reflects the lack of an atmospheric pZn source for this remote open-ocean region, consistent with previous observations of low dissolved aluminium (dAl), a tracer of atmospheric dust supply, along this transect (Barrett et al., 2018). A localised pZn_{lith} signal was however evident above the mid-ocean ridge at 50°S where pZn_{lith} was 0.01 nmol kg^{-1}, the highest estimate along the transect. The pZn_{lith} maximum occurred in the deepest sample (3500 m), roughly 500 m above the seafloor, and therefore resuspension of seafloor sediment seems an unlikely source. A more probable source was hydrothermal fluids expelled from the mid-ocean ridge considering that highest concentrations of pAl (6 nmol kg^{-1}) and particulate iron (pFe; 2 nmol kg^{-1}), two hydrothermal indicator elements, were also measured in this sample. Once ejected, hydrothermally derived pZn may either sink as Zn-rich particles to the seafloor (German et al., 1991) or dissociate to dZn followed by lateral advection (Roshan et al., 2016). The latter mechanism therefore has the potential to influence deep dZn distributions although this was not evident in our data where the dZn:$Si(OH)_4$ ratio ($Si(OH)_4$ is not a hydrothermally derived element), in the sample was 0.069 mmol mol^{-1}, consistent with deep (< 2000 m) dZn:$Si(OH)_4$ for the whole transect (0.066 ± 0.003 mmol mol^{-1}).

The elevated pZn_{lith} found in subsurface water masses of the STZ, with a core of 0.009 nmol kg^{-1} at 800 m, may reflect the influence of ARC waters which were sampled during at our STZ station (Fig. 7). The ARC, which extends between surface and > 1500 m (Lutjeharms and Ansorge, 2001), is supplied by the AC which flows along the south east African continental margin before retroflecting south of Africa and flowing eastward, often in close association with the STF. The AC is characterised by massive lithogenic inputs of pAl and pFe, up to 673 and 224 nmol kg^{-1}, respectively, through interaction with the African continental shelf (Grand et al., 2015) and potentially entrains significant amounts of pZn (1.10 nmol kg^{-1} of pZn_{lith} using the Zn/Al_{UCC} ratio in Eq. (2)) which are ultimately inherited by the ARC. The lithogenic signal is however diluted with distance from the shelf source (Barrett et al., 2018; Grand et al., 2015) and particles may be remineralised or sink to subsurface waters during the timescales taken for the AC to retroflect and

return as the ARC (on the order of weeks; Lutjeharms and Ansorge, 2001). Ultimately, the enriched pZn_{lith} in subsurface waters at the northern stations may reflect the signature of ARC enriched in lithogenic material derived from the AC, an observation consistent with sustained high Al in subsurface waters further east (Grand et al., 2015). However, the remineralisation of the high pZn_{lith} in the STZ is not likely to influence subsurface dZn significantly considering that pZn_{lith} is negligible compared to dZn (> 2%).

4.6. Inhibited mixing south of the Indian ridge

Highest concentrations of dZn were measured in deep waters south of the mid-ocean ridge (hereafter Indian ridge). South of the Indian ridge (St. 50°S and 56°S), dZn was 9.07 ± 0.06 (n = 2) and 8.27 ± 0.18 nmol kg^{-1} (n = 2) below 3000 m (Fig. 2A), respectively while to the north of the Indian ridge (St. 48°S and 45°S), dZn was lower (6.84 ± 0.23 nmol kg^{-1}; n = 4). While dZn data for bottom waters in the Southern Ocean is extremely limited, our concentrations appear higher compared to concentrations measured below 3000 m (7.25 ± 0.58 nmol kg^{-1}; n = 6) and nearer to the AABW formation region (Zhao et al., 2014). The higher dZn in deep waters south of the Indian ridge was associated with the highest measured $Si(OH)_4$ (129 ± 2 μmol kg^{-1}) suggesting that the resuspension of opal-rich sediment may be contributing to elevated dZn and $Si(OH)_4$ as observed in the South Atlantic (Wyatt et al., 2014). While the deepest sampled depth at 50°S was in close proximity to the seafloor, resuspension of opal-rich sediment is unlikely at 56°S where the deepest sampled depth (3500 m) was well above the seafloor depth (~5500 m; Fig. 2A). Instead we propose that inhibited mixing to the south of the Indian ridge may increase the residence time of 'pure' AABW thereby allowing for the accumulation of dZn and $Si(OH)_4$ and likely other nutrients which show deep water maxima. Pure AABW here refers to AABW in the absence of significant mixing/dilution with other water masses (> 75% AABW). Importantly, the long residence time of dZn (3000–11,000 years; Little et al. (2014); Roshan et al. (2016)) and $Si(OH)_4$ (~10,000 years; Tréguer and De La Rocha (2013)) in the ocean, longer than the timescales used to measure oceanic overturning circulation (centennial timescales; Matsumoto (2007)), supports the idea of nutrient accumulation in bottom waters. Pure bottom waters in this region have been shown to not extend north of the Indian ridge (Anilkumar et al., 2006) and that deep waters north of the Indian ridge are instead an altered variety of LCDW resulting from diapycnal mixing between pure AABW and LCDW (Mantyla and Reid, 1995). In an effort to further validate these observations, we performed an eOMP analysis which computes the contributions of pre-defined end-member water masses to each measured sample (see Section 2.7). Consistent with our hypothesis, results of the eOMP analysis suggest that samples below 3000 m south of the Indian ridge are composed predominantly of AABW, up to 85% at the deepest sampled depth (Fig. 8). It therefore appears plausible that inhibited mixing and increased residence times of deep waters south of the Indian ridge may contribute to elevated dZn and $Si(OH)_4$ concentrations in this region. We do however acknowledge that more deep water measurements are necessary to confirm this hypothesis.

5. Conclusion

Winter measurements of dZn and pZn are presented along the 30°E longitude in the Indian Sector of the Southern Ocean. The results provided the unique opportunity to investigate Zn cycling over seasonal cycles and to gain insights into processes driving the exchange between dissolved and particulate phases in a region which is extremely data scarce. Vertical profiles of dZn showed surface depletions and progressive enrichments with depth and contrasted profiles of pZn which showed enrichments near the surface followed be a decline in concentration with depth. These characteristics reflect biological uptake in surface waters and remineralisation in the subsurface. Seasonal variations in Zn distributions were most apparent at the higher latitudes where winter dZn was higher, and pZn was lower, than spring and summer measurements owing to reduced biological uptake. Additionally, deep winter mixing may preferentially resupply dZn (relative to PO_4) to winter surface waters through access to dZn-enriched (from diatom remineralisation) waters found below the spring/summer mixed layers. The composition of pZn was dominated by biogenic pZn although lithogenic contributions were observed at depth over the Indian ridge, likely a hydrothermal signal, and at mid-depths in the STZ, potentially from advection of Agulhas waters rich in lithogenic material derived from the African continental margin. Calculated vertical attenuation factors for our particulate data suggest Zn has a longer remineralisation length scale than P and provides a mechanism explaining the observed differences in their respective dissolved phase vertical distributions, i.e., the deep dZn maxima and intermediate PO_4 maxima result in a curvilinear relationship. There were however distinct differences in Zn cycling across the transect. In the AAZ for example, the high surface pZn:P ratios, characteristic of Southern Ocean diatoms, was driven by increased dZn availability and potentially Fe-limitation. Furthermore, pZn:P in the AAZ did not vary significantly with depth, in contrast to the lower latitude stations where pZn:P increased significantly with depth. The high pZn:P throughout the upper water column of the AAZ indicates the export of diatom cells below the winter mixed layer, as hypothesised by Vance et al. (2017), where rigorous mixing may resolve the strong linear dZn-$Si(OH)_4$ correlation in deep waters despite these elements being located in separate components of the diatom cell. Lastly, inhibited mixing leading to increased residence times of bottom waters south of the Indian ridge may partly explain the elevated dZn and $Si(OH)_4$ in comparison to deep waters to the north of the Indian ridge.

6. Acknowledgements

We would like to thank the South African National Antarctic Programme (SANAP) as well as Captain Knowledge Bengu and the crew of the R/V SA Agulhas II for their professionalism and support during the winter 2017 voyage. We acknowledge Chief Scientist Marcello Vichi and all the participants involved in the expedition. We are grateful to the “Iron” team for their help in collecting trace-clean seawater samples. We would like to thank Eric Achterberg, Angela Milne, Andrew Bowie, Gideon Henderson, Yoshiki Sohrin, Maeve Lohan and Michael Ellwood for allowing permission to use data that are not published outside of the IDP2017. Finally, we thank three reviewers for their insightful discussions, the results of which improved this manuscript. Ryan Cloete was supported through the National Research Foundation

(NRF) Innovation PhD studentship. This research was supported by NRF grants (UID# 93069, 105826 and 110715) to A.R. S.F. acknowledges funding from NRF (UID 111210, 110731).

7. References

Anderson, L.A., Sarmiento, J.L., 1994. Redfield ratios of remineralization determined by nutrient data analysis. Global Biogeochem. Cycles 8, 65–80. https://doi.org/https://doi.org/10.1029/93GB03318

Anderson, R.F., 2020. GEOTRACES: Accelerating Research on the Marine Biogeochemical Cycles of Trace Elements and Their Isotopes. Ann. Rev. Mar. Sci. 12, 48–85. https://doi.org/https://doi.org/10.1146/annurev-marine-010318-095123

Anilkumar, N., Luis, A.J., Somayajulu, Y.K., Ramesh Babu, V., Dash, M.K., Pednekar, S.M., Babu, K.N., Sudhakar, M., Pandey, P.C., 2006. Fronts, water masses and heat content variability in the Western Indian sector of the Southern Ocean during austral summer 2004. J. Mar. Syst. 63, 20–34. https://doi.org/10.1016/j.jmarsys.2006.04.009

Baars, O., Croot, P.L., 2011. The speciation of dissolved zinc in the Atlantic sector of the Southern Ocean. Deep. Res. Part II Top. Stud. Oceanogr. 58, 2720–2732. https://doi.org/10.1016/j.dsr2.2011.02.003

Barrett, P.M., Resing, J.A., Grand, M.M., Measures, C.I., Landing, W.M., 2018. Trace element composition of suspended particulate matter along three meridional CLIVAR sections in the Indian and Southern Oceans: Impact of scavenging on Al distributions. Chem. Geol. 502, 15–28. https://doi.org/10.1016/j.chemgeo.2018.06.015

Belkin, I.M., Gordon, A.L., 1996. Southern Ocean fronts from the Greewich meridian to Tasmania. J. Geophys. Res. 101, 3675–3696. https://doi.org/https://doi.org/10.1029/95JC02750

Boyd, P.W., Ellwood, M.J., Tagliabue, A., Twining, B.S., 2017. Biotic and abiotic retention, recycling and remineralization of metals in the ocean. Nat. Publ. Gr. 10, 167–173. https://doi.org/10.1038/ngeo2876

Brand, L.E., Sunda, W.G., Guillard, R.R.L., 1983. Limitation of marine phytoplankton reproductive rates by zinc, manganese, and iron. Limnol. Oceanogr. 28, 1182–1198. https://doi.org/https://doi.org/10.4319/lo.1983.28.6.1182

Broecker, W.S., 1991. The Great Ocean Conveyor. Oceanography 4, 79–89. https://doi.org/https://doi.org/10.5670/oceanog.1991.07

Bruland, K.W., 1980. Oceanographic distributions of cadmium, zinc, nickel, and copper in the North Pacific. Earth Planet. Sci. Lett. 47, 176–198. https://doi.org/10.1016/0012-821X(80)90035-7

Butler, E.C. V, O'Sullivan, J.E., Watson, R.J., Bowie, A.R., Remenyi, T.A., Lannuzel, D., 2013. Trace metals Cd, Co, Cu, Ni, and Zn in waters of the subantarctic and Polar Frontal Zones south of Tasmania during the "SAZ-Sense" project. Mar. Chem. 148, 63–76. https://doi.org/10.1016/j.marchem.2012.10.005

Carter, B.R., Talley, L.D., Dickson, A.G., 2014. Mixing and remineralization in waters detrained from the surface into Subantarctic Mode Water and Antarctic Intermediate Water in the southeastern Pacific. J. Geophys. Res. Ocean. 119, 4001–4028. https://doi.org/doi:10.1002/ 2013JC009355

Castro, C.G., Pérez, F.F., Holley, S.E., Ríos, A.F., 1998. Chemical characterisation and modelling of water masses in the Northeast Atlantic. Prog. Oceanogr. 41, 249–279. https://doi.org/https://doi.org/10.1016/S0079-6611(98)00021-4

Cloete, R., Loock, J.C., Mtshali, T., Fietz, S., Roychoudhury, A.N., 2019. Winter and summer distributions of Copper, Zinc and Nickel along the International GEOTRACES Section GIPY05: Insights into deep winter mixing. Chem. Geol. 511, 342–357.

https://doi.org/10.1016/j.chemgeo.2018.10.023

Cloete, R., Loock, J.C., van Horsten, N.R., Fietz, S., Mtshali, T.N., Planquette, H., Roychoudhury, A.N., 2021. Winter biogeochemical cycling of dissolved and particulate cadmium in the Indian sector of the Southern Ocean (GEOTRACES GIpr07 transect). Front. Mar. Sci. in review.

Coale, K.H., Michael Gordon, R., Wang, X., 2005. The distribution and behavior of dissolved and particulate iron and zinc in the Ross Sea and Antarctic circumpolar current along 170°W. Deep Sea Res. Part I Oceanogr. Res. Pap. 52, 295–318. https://doi.org/10.1016/j.dsr.2004.09.008

Conway, T.M., John, S.G., 2015. The cycling of iron, zinc and cadmium in the North East Pacific Ocean - Insights from stable isotopes. Geochim. Cosmochim. Acta 164, 262–283. https://doi.org/10.1016/j.gca.2015.05.023

Croot, P.L., Baars, O., Streu, P., 2011. The distribution of dissolved zinc in the Atlantic sector of the Southern Ocean. Deep Sea Res. Part II Top. Stud. Oceanogr. 58, 2707–2719. https://doi.org/10.1016/j.dsr2.2010.10.041

Cullen, J.T., Chase, Z., Coale, K.H., Fitzwater, S.E., Sherrell, R.M., 2003. Effect of iron limitation on the cadmium to phosphorous ratio of natural phytoplankton assemblages from the Southern Ocean. Limnol. Oceanogr. 48, 1079–1087. https://doi.org/10.4319/lo.2003.48.3.1079

Cutter, G., Casciotti, K., Croot, P., Geibert, W., Heimbürger, L.-E., Lohan, M., Planquette, H., van de Flierdt, T., 2017. Sampling and Sample-handling Protocols for GEOTRACES Cruises. Version 3, August 2017. Toulouse, France. https://doi.org/httdx.doi.org/10.25607/OBP-2 Collections

de Jong, E., Vichi, M., Mehlmann, C.B., Eayrs, C., De Kock, W., Moldenhauer, M., Audh, R.R., 2018. Sea Ice conditions within the Antarctic Marginal Ice Zone in winter 2017, onboard the SA Agulhas II, in: PANGAEA. University of Cape Town. https://doi.org/https://doi.org/10.1594/PANGAEA.885211

Ellwood, M.J., 2008. Wintertime trace metal (Zn, Cu, Ni, Cd, Pb and Co) and nutrient distributions in the Subantarctic Zone between 40-52°S; 155-160°E. Mar. Chem. 112, 107–117. https://doi.org/10.1016/j.marchem.2008.07.008

Ellwood, M.J., Hunter, K.A., 2000. The incorporation of zinc and iron into the frustule of the marine diatom Thalassiosira pseudonana. Limnol. Oceanogr. 45, 1517–1524. https://doi.org/10.4319/lo.2000.45.7.1517

Ellwood, M.J., Strzepek, R., Chen, X., Trull, T.W., Boyd, P.W., 2020. Some observations on the biogeochemical cycling of zinc in the Australian sector of the Southern Ocean: A dedication to Keith Hunter. Mar. Freshw. Res. 71, 355–373. https://doi.org/10.1071/MF19200

German, C.R., Campbell, A.C., Edmond, J.M., 1991. Hydrothermal scavenging at the Mid-Atlantic Ridge: Modification of trace element dissolved fluxes. Earth Planet. Sci. Lett. 107, 101–114. https://doi.org/10.1016/0012-821X(91)90047-L

Gordon, A.L., Weiss, R.F., Smethie, W.M., Warner, M.J., 1992. Thermocline and intermediate water communication between the south Atlantic and Indian oceans. J. Geophys. Res. 97, 7223–7240. https://doi.org/https://doi.org/10.1029/92JC00485

Grand, M.M., Measures, C.I., Hatta, M., Morton, P.L., Barrett, P., Milne, A., Resing, J.A., Landing, W.M., 2015. The impact of circulation and dust deposition in controlling the distributions of dissolved Fe and Al in the south Indian subtropical gyre. Mar. Chem. 176, 110–125. https://doi.org/10.1016/j.marchem.2015.08.002

Grasshoff, K., 1983. Automated chemical analysis, in: Grasshoff, K., Ernhardt, M., Kremling, K. (Eds.), Methods of Seawater Analysis. Verlag Chemie Weinhein, New York, pp. 263–289. https://doi.org/10.1002/9783527613984

693 Jackson, S.L., Spence, J., Janssen, D.J., Ross, A.R.S., Cullen, J.T., 2018. Determination of Mn, Fe, Ni,
694 Cu, Zn, Cd and Pb in seawater using offline extraction and triple quadrupole ICP-MS/MS. J. Anal.
695 At. Spectrom. 33, 304–313. https://doi.org/10.1039/c7ja00237h

696 Janssen, D.J., Cullen, J.T., 2015. Decoupling of zinc and silicic acid in the subarctic northeast Pacific
697 interior. Mar. Chem. 177, 124–133. https://doi.org/10.1016/j.marchem.2015.03.014

698 Janssen, D.J., Sieber, M., Ellwood, M.J., Conway, T.M., Barrett, P.M., Chen, X., de Souza, G.F., Hassler,
699 C.S., Jaccard, S.L., 2020. Trace metal and nutrient dynamics across broad biogeochemical gradients
700 in the Indian and Pacific sectors of the Southern Ocean. Mar. Chem. 221, 103773.
701 https://doi.org/10.1016/j.marchem.2020.103773

702 John, S.G., Conway, T.M., 2014. A role for scavenging in the marine biogeochemical cycling of zinc and
703 zinc isotopes. Earth Planet. Sci. Lett. 394, 159–167. https://doi.org/10.1016/j.epsl.2014.02.053

704 Karstensen, J., Tomczak, M., 1998. Age determination of mixed water masses using CFC and oxygen
705 Data. J. Geophys. Res. 103, 18599–18609. https://doi.org/https://doi.org/10.1029/98JC00889

706 Lam, P.J., Marchal, O., 2015. Insights into Particle Cycling from Thorium and Particle Data. Ann. Rev.
707 Mar. Sci. 7, 159–184. https://doi.org/10.1146/annurev-marine-010814-015623

708 Little, S.H., Vance, D., Walker-Brown, C., Landing, W.M., 2014. The oceanic mass balance of copper
709 and zinc isotopes, investigated by analysis of their inputs, and outputs to ferromanganese oxide
710 sediments. Geochim. Cosmochim. Acta 125, 673–693. https://doi.org/10.1016/j.gca.2013.07.046

711 Liu, M., Tanhua, T., 2021. Water masses in the Atlantic Ocean: Characteristics and distributions. Ocean
712 Sci. 17, 463–486. https://doi.org/https://doi.org/10.5194/os-17-463-2021

713 Löscher, B.M., 1999. Relationships among Ni, Cu, Zn, and major nutrients in the Southern Ocean. Mar.
714 Chem. 67, 67–102. https://doi.org/10.1016/S0304-4203(99)00050-X

715 Lutjeharms, J.R.E., Ansorge, I.J., 2001. The Agulhas Return Current. J. Mar. Syst. 30, 115–138.
716 https://doi.org/https://doi.org/10.1016/S0924-7963(01)00041-0

717 Mantyla, A.W., Reid, J.L., 1995. On the origins of deep and bottom waters of the Indian Ocean. J.
718 Geophys. Res. Ocean. 100, 2417–2439. https://doi.org/https://doi.org/10.1029/94JC02564

719 Martin, J.H., Knauer, G.A., Karl, D.M., Broenkow, W.W., 1987. VERTEX: carbon cycling in the
720 northeast Pacific. Deep Sea Res. Part A, Oceanogr. Res. Pap. 34, 267–285.
721 https://doi.org/10.1016/0198-0149(87)90086-0

722 Matsumoto, K., 2007. Radiocarbon-based circulation age of the world oceans. J. Geophys. Res. Ocean.
723 112, 1–7. https://doi.org/10.1029/2007JC004095

724 Middag, R., de Baar, H.J.W., Bruland, K.W., 2019. The Relationships Between Dissolved Zinc and Major
725 Nutrients Phosphate and Silicate Along the GEOTRACES GA02 Transect in the West Atlantic
726 Ocean. Global Biogeochem. Cycles 33, 63–84. https://doi.org/10.1029/2018GB006034

727 Middag, R., van Heuven, S.M.A.C., Bruland, K.W., de Baar, H.J.W., 2018. The relationship between
728 cadmium and phosphate in the Atlantic Ocean unravelled. Earth Planet. Sci. Lett. 492, 79–88.
729 https://doi.org/10.1016/j.epsl.2018.03.046

730 Morel, F.M.M., Hudson, R.J.M., Price, N.M., 1991. Limitation of productivity by trace metals in the sea.
731 Limnol. Oceanogr. 36, 1742–1755. https://doi.org/10.4319/lo.1991.36.8.1742

732 Morel, F.M.M., Price, N.M., 2003. The Biogeochemical Cycles of Trace Metals in the Oceans. Science.
733 300, 944–947. https://doi.org/10.1126/science.1083545

734 Morel, F.M.M., Reinfelder, J.R., Roberts, S.B., Chamberlain, C.P., Lee, J.G., Yee, D., 1994. Zinc and
735 carbon co-limitation of marine phytoplankton. Nature 369, 740–742.
736 https://doi.org/https://doi.org/10.1038/369740a0

Orsi, A.H., Johnson, G.C., Bullister, J.L., 1999. Circulation, mixing, and production of Antarctic Bottom Water. Prog. Oceanogr. 43, 55–109. https://doi.org/10.1016/S0079-6611(99)00004-X

Orsi, A.H., Whitworth, T., Nowlin, W.D., 1995. On the meridional extent and fronts of the Antarctic Circumpolar Current. Deep. Res. Part I 42, 641–673. https://doi.org/10.1016/0967-0637(95)00021-W

Perez, F.F., Mouriño, C., Fraga, F., Rios, A.F., 1993. Displacement of water masses and remineralization rates off the Iberian Peninsula by nutrient anomalies. J. Mar. Syst. 51, 869–892. https://doi.org/https://doi.org/10.1357/0022240933223891

Planquette, H., Sherrell, R.M., 2012. Sampling for particulate trace element determination using water sampling bottles: methodology and comparison to in situ pumps. Limnol. Oceanogr. Methods 10, 367–388. https://doi.org/10.4319/lom.2012.10.367

Pollard, R.T., Lucas, M.I., Read, J.F., 2002. Physical controls on biogeochemical zonation in the Southern Ocean. Deep. Res. Part II Top. Stud. Oceanogr. 49, 3289–3305. https://doi.org/10.1016/S0967-0645(02)00084-X

Quay, P., Cullen, J., Landing, W., Morton, P., 2015. Processes controlling the distributions of Cd and PO4 in the ocean. Global Biogeochem. Cycles 29, 830–841. https://doi.org/10.1002/2014GB004998

Rapp, I., Schlosser, C., Rusiecka, D., Gledhill, M., Achterberg, E.P., 2017. Automated preconcentration of Fe, Zn, Cu, Ni, Cd, Pb, Co, and Mn in seawater with analysis using high-resolution sector field inductively- coupled plasma mass spectrometry. Anal. Chim. Acta 976, 1–13. https://doi.org/10.1016/j.aca.2017.05.008

Raven, J.A., 2013. The evolution of autotrophy in relation to phosphorus requirement. J. Exp. Bot. 64, 4023–4046. https://doi.org/10.1093/jxb/ert306

Roshan, S., Wu, J., Jenkins, W.J., 2016. Long-range transport of hydrothermal dissolved Zn in the tropical South Pacific. Mar. Chem. 183, 25–32. https://doi.org/10.1016/j.marchem.2016.05.005

Rudnick, R.L., Gao, S., 2013. Composition of the Continental Crust, 2nd ed, Treatise on Geochemistry: Second Edition. Elsevier Ltd. https://doi.org/10.1016/B978-0-08-095975-7.00301-6

Saito, M.A., Goepfert, T.J., 2008. Zinc – cobalt colimitation of Phaeocystis antarctica 53, 1–11. https://doi.org/https://doi.org/10.4319/lo.2008.53.1.0266

Sarmiento, J.L., Gruber, N., Brzezinski, M.A., Dunne, J.P., 2004. High-latitude controls of thermocline nutrients and low latitude biological productivity. Nature 427, 56–60. https://doi.org/10.1038/nature10605

Schlitzer, R., 2020. Ocean Data View. https://doi.org/10.1017/CBO9781107415324.004

Schlitzer, R., Anderson, R.F., Dodas, E.M., Lohan, M., Geibert, W., Tagliabue, A., Bowie, A., Jeandel, C., Maldonado, M.T., Landing, W.M., Cockwell, D., Abadie, C., Abouchami, W., Achterberg, E.P., Agather, A., Aguliar-Islas, A., van Aken, H.M., Andersen, M., Archer, C., Auro, M., de Baar, H.J., Baars, O., Baker, A.R., Bakker, K., Basak, C., Baskaran, M., Bates, N.R., Bauch, D., van Beek, P., Behrens, M.K., Black, E., Bluhm, K., Bopp, L., Bouman, H., Bowman, K., Bown, J., Boyd, P., Boye, M., Boyle, E.A., Branellec, P., Bridgestock, L., Brissebrat, G., Browning, T., Bruland, K.W., Brumsack, H.J., Brzezinski, M., Buck, C.S., Buck, K.N., Buesseler, K., Bull, A., Butler, E., Cai, P., Mor, P.C., Cardinal, D., Carlson, C., Carrasco, G., Casacuberta, N., Casciotti, K.L., Castrillejo, M., Chamizo, E., Chance, R., Charette, M.A., Chaves, J.E., Cheng, H., Chever, F., Christl, M., Church, T.M., Closset, I., Colman, A., Conway, T.M., Cossa, D., Croot, P., Cullen, J.T., Cutter, G.A., Daniels, C., Dehairs, F., Deng, F., Dieu, H.T., Duggan, B., Dulaquais, G., Dumousseaud, C., Echegoyen-Sanz, Y., Edwards, R.L., Ellwood, M., Fahrbach, E., Fitzsimmons, J.N., Russell Flegal, A., Fleisher, M.Q., van de Flierdt, T., Frank, M., Friedrich, J., Fripiat, F., Fröllje, H., Galer, S.J.G., Gamo, T., Ganeshram, R.S., Garcia-Orellana, J., Garcia-Solsona, E., Gault-Ringold, M., George, E.,

Gerringa, L.J.A., Gilbert, M., Godoy, J.M., Goldstein, S.L., Gonzalez, S.R., Grissom, K., Hammerschmidt, C., Hartman, A., Hassler, C.S., Hathorne, E.C., Hatta, M., Hawco, N., Hayes, C.T., Heimbürger, L.E., Helgoe, J., Heller, M., Henderson, G.M., Henderson, P.B., van Heuven, S., Ho, P., Horner, T.J., Hsieh, Y. Te, Huang, K.F., Humphreys, M.P., Isshiki, K., Jacquot, J.E., Janssen, D.J., Jenkins, W.J., John, S., Jones, E.M., Jones, J.L., Kadko, D.C., Kayser, R., Kenna, T.C., Khondoker, R., Kim, T., Kipp, L., Klar, J.K., Klunder, M., Kretschmer, S., Kumamoto, Y., Laan, P., Labatut, M., Lacan, F., Lam, P.J., Lambelet, M., Lamborg, C.H., Le Moigne, F.A.C., Le Roy, E., Lechtenfeld, O.J., Lee, J.M., Lherminier, P., Little, S., López-Lora, M., Lu, Y., Masque, P., Mawji, E., Mcclain, C.R., Measures, C., Mehic, S., Barraqueta, J.L.M., van der Merwe, P., Middag, R., Mieruch, S., Milne, A., Minami, T., Moffett, J.W., Moncoiffe, G., Moore, W.S., Morris, P.J., Morton, P.L., Nakaguchi, Y., Nakayama, N., Niedermiller, J., Nishioka, J., Nishiuchi, A., Noble, A., Obata, H., Ober, S., Ohnemus, D.C., van Ooijen, J., O'Sullivan, J., Owens, S., Pahnke, K., Paul, M., Pavia, F., Pena, L.D., Peters, B., Planchon, F., Planquette, H., Pradoux, C., Puigcorbé, V., Quay, P., Queroue, F., Radic, A., Rauschenberg, S., Rehkämper, M., Rember, R., Remenyi, T., Resing, J.A., Rickli, J., Rigaud, S., Rijkenberg, M.J.A., Rintoul, S., Robinson, L.F., Roca-Martí, M., Rodellas, V., Roeske, T., Rolison, J.M., Rosenberg, M., Roshan, S., Rutgers van der Loeff, M.M., Ryabenko, E., Saito, M.A., Salt, L.A., Sanial, V., Sarthou, G., Schallenberg, C., Schauer, U., Scher, H., Schlosser, C., Schnetger, B., Scott, P., Sedwick, P.N., Semiletov, I., Shelley, R., Sherrell, R.M., Shiller, A.M., Sigman, D.M., Singh, S.K., Slagter, H.A., Slater, E., Smethie, W.M., Snaith, H., Sohrin, Y., Sohst, B., Sonke, J.E., Speich, S., Steinfeldt, R., Stewart, G., Stichel, T., Stirling, C.H., Stutsman, J., Swarr, G.J., Swift, J.H., Thomas, A., Thorne, K., Till, C.P., Till, R., Townsend, A.T., Townsend, E., Tuerena, R., Twining, B.S., Vance, D., Velazquez, S., Venchiarutti, C., Villa-Alfageme, M., Vivancos, S.M., Voelker, A.H.L., Wake, B., Warner, M.J., Watson, R., van Weerlee, E., Alexandra Weigand, M., Weinstein, Y., Weiss, D., Wisotzki, A., Woodward, E.M.S., Wu, J., Wu, Y., Wuttig, K., Wyatt, N., Xiang, Y., Xie, R.C., Xue, Z., Yoshikawa, H., Zhang, J., Zhang, P., Zhao, Y., Zheng, L., Zheng, X.Y., Zieringer, M., Zimmer, L.A., Ziveri, P., Zunino, P., Zurbrick, C., 2018. The GEOTRACES Intermediate Data Product 2017. Chem. Geol. 493, 210–223. https://doi.org/10.1016/j.chemgeo.2018.05.040

Shaked, Y., Xu, Y., Leblanc, K., Morel, F.M.M., 2006. Zinc availability and alkaline phosphatase activity in Emiliania huxleyi : Implications for Zn – P co-limitation in the ocean. Limnol. Ocean. 51, 299–309. https://doi.org/https://doi.org/10.4319/lo.2006.51.1.0299

Sieber, M., Conway, T.M., Souza, G.F. De, Hassler, C.S., Ellwood, M.J., Vance, D., 2019. Cycling of zinc and its isotopes across multiple zones of the Southern Ocean : Insights from the Antarctic Circumnavigation Expedition. Geochim. Cosmochim. Acta. https://doi.org/10.1016/j.gca.2019.09.039

Souza, G.F. De, Khatiwala, S.P., Hain, M.P., Little, S.H., Vance, D., 2018. On the origin of the marine zinc – silicon correlation. Earth Planet. Sci. Lett. 492, 22–34. https://doi.org/10.1016/j.epsl.2018.03.050

Sunda, W.G., Huntsman, S.A., 1996. Antagonisms between cadmium and zinc toxicity and manganese limitation in a coastal diatom. Limnol. Ocean. 41, 373–387. https://doi.org/https://doi.org/10.4319/lo.1996.41.3.0373

Sunda, W.G., Huntsman, S.A., 1995. Cobalt and zinc interreplacement in marine phytoplankton: Biological and geochemical implications. Limnol. Oceanogr. 40, 1404–1417. https://doi.org/10.4319/lo.1995.40.8.1404

Tagliabue, A., Sallée, J.B., Bowie, A.R., Lévy, M., Swart, S., Boyd, P.W., 2014. Surface-water iron supplies in the Southern Ocean sustained by deep winter mixing. Nat. Geosci. 7, 314–320. https://doi.org/10.1038/ngeo2101

Takahashi, T., Broecker, W.S., Langer, S., 1985. Redfield ratio based on chemical data from isopycnal surfaces. J. Geophys. Res. 90, 6907–6924. https://doi.org/https://doi.org/10.1029/JC090iC04p06907

Tomczak, M., 1999. Some historical, theoretical and applied aspects of quantitative water mass analysis.

J. Mar. Res. 57, 275–303. https://doi.org/https://doi.org/10.1357/002224099321618227

Tréguer, P.J., De La Rocha, C.L., 2013. The World Ocean Silica Cycle. Ann. Rev. Mar. Sci. 5, 477–501. https://doi.org/10.1146/annurev-marine-121211-172346

Twining, B.S., Baines, S.B., 2013. The trace metal composition of marine phytoplankton. Ann. Rev. Mar. Sci. 5, 191–215. https://doi.org/10.1146/annurev-marine-121211-172322

Twining, B.S., Baines, S.B., Fisher, N.S., 2004. Element stoichiometries of individual plankton cells collected during the Southern Ocean Iron Experiment (SOFeX). Limnol. Oceanogr. 49, 2115–2128. https://doi.org/10.4319/lo.2004.49.6.2115

Twining, B.S., Baines, S.B., Fisher, N.S., Maser, J., Vogt, S., Jacobsen, C., Tovar-Sanchez, A., Sañudo-Wilhelmy, S.A., 2003. Quantifying trace elements in individual aquatic protist cells with a synchrotron X-ray fluorescence microprobe. Anal. Chem. 75, 3806–3816. https://doi.org/10.1021/ac034227z

Twining, B.S., Nodder, S.D., King, A.L., Hutchins, D.A., Lecleir, G.R., Debruyn, J.M., Maas, E.W., Vogt, S., Wilhelm, S.W., Boyd, P.W., 2014. Differential remineralization of major and trace elements in sinking diatoms. Limnol. Oceanogr. 59, 689–704. https://doi.org/10.4319/lo.2014.59.3.0689

van Aken, H.M., Ridderinkhof, H., de Ruijter, W.P.M., 2004. North Atlantic deep water in the south-western Indian Ocean. Deep Sea Res. Part I Oceanogr. Res. Pap. 51, 755–776. https://doi.org/10.1016/j.dsr.2004.01.008

Van Horsten, N.R., Planquette, H., Sarthou, G., Ryan-Keogh, T.J., Mtshali, T.N., Roychoudhury, A., Bucciarelli, E., 2021. Early winter barium excess in the Southern Indian Ocean as an annual remineralisation proxy (GEOTRACES GIPr07 cruise). Biogeosciences in review. https://doi.org/https://doi.org/10.5194/bg-2021-42

Vance, D., Little, S.H., De Souza, G.F., Khatiwala, S., Lohan, M.C., Middag, R., 2017. Silicon and zinc biogeochemical cycles coupled through the Southern Ocean. Nat. Geosci. 10, 202–206. https://doi.org/10.1038/ngeo2890

Wang, R.M., Archer, C., Bowie, A.R., Vance, D., 2018. Zinc and nickel isotopes in seawater from the Indian Sector of the Southern Ocean: The impact of natural iron fertilization versus Southern Ocean hydrography and biogeochemistry. Chem. Geol. https://doi.org/10.1016/j.chemgeo.2018.09.010

Weber, T., John, S., Tagliabue, A., Devries, T., 2018. Biological uptake and reversible scavenging of zinc in the global ocean. Science (80-.). 361, 72–76. https://doi.org/10.1126/science.aap8532

Weir, I., Fawcett, S., Smith, S., Walker, D., Bornman, T., Fietz, S., 2020. Winter biogenic silica and diatom distributions in the Indian sector of the Southern Ocean. Deep. Res. Part I Oceanogr. Res. Pap. 166, 103421. https://doi.org/10.1016/j.dsr.2020.103421

Wolters, M., 2002. Quickchem Method 31-114-27-1-D – Silicate in Brackish or Seawater. Colorado, USA.

Wyatt, N.J., Milne, A., Woodward, E.M.S., Rees, A.P., Browning, T.J., Bouman, H.A., Worsfold, P.J., Lohan, M.C., 2014. Biogeochemical cycling of dissolved zinc along the GEOTRACES South Atlantic transect GA10 at 40°S. Global Biogeochem. Cycles 28, 44–56. https://doi.org/10.1002/2013GB004637

Xie, R.C., Galer, S.J.G., Abouchami, W., Rijkenberg, M.J.A., De Jong, J., De Baar, H.J.W., Andreae, M.O., 2015. The cadmium-phosphate relationship in the western South Atlantic - The importance of mode and intermediate waters on the global systematics. Mar. Chem. 177, 110–123. https://doi.org/10.1016/j.marchem.2015.06.011

Zhao, Y., Vance, D., Abouchami, W., de Baar, H.J.W., 2014. Biogeochemical cycling of zinc and its

isotopes in the Southern Ocean. Geochim. Cosmochim. Acta 125, 653–672.
https://doi.org/10.1016/j.gca.2013.07.045

List of Tables

Table 1. *Results from the ICP-MS analysis of GEOTRACES SAFE D2, GSC and GSP seawater reference materials, NASS-7 certified seawater reference material and our own WISOS internal reference seawater are compared with respective consensus values. Consensus values for SAFe D2 as of 2013 and GSC and GSP as of 2019. Certified values for NASS-7 as of 2018. Calibrated mean values for WISOS calculated by repeat analysis (n > 10) of a large volume surface seawater sample collected from 55°S; 28°E. Instrument and method blanks as well as ICP-MS detection limits are also shown.*

	dZn nmol kg^{-1}
SAFe D2	
Consensus	7.43 ± 0.25
Measured (n = 4)	7.23 ± 0.25
GSC	
Consensus	1.40 ± 0.10
Measured (n = 5)	1.41 ± 0.10
GSP	
Consensus	0.03 ± 0.05
Measured (n = 5)	0.10 ± 0.02
NASS-7	
Certified	6.27 ± 1.22
Measured (n = 5)	6.59 ± 0.07
WISOS reference seawater	
TracEx Calibration (n = 10)	9.67 ± 0.23
Measured (n > 30)	9.63 ± 0.24
Blanks	
Instrument (n = 5)	0.07 ± 0.01
Method (n = 5)	0.09 ± 0.01
Limit of Detection (n = 5)	0.02

889 **Table 2**. *Results for pZn and P from the ICP-MS analysis of PACS 3, MESS 4 and BCR 414 certified*
890 *references materials. Filter blanks as well as ICP-MS limit of detection are also shown.*

	pZn	**P**
	mmol kg^{-1}	*mmol kg^{-1}*
PACS 3		
Certified	5.80 ± 0.23	29.38 ± 2.91
Measured	6.24 ± 0.72	29.41 ± 0.31
% recovery	108	100
MESS 4		
Certified	2.25 ± 0.09	33.58 ± 5.17
Measured	2.25 ± 0.59	35.58 ± 0.51
% recovery	100	106
BCR 414		
Certified	1.71 ± 0.04	428.84 ± 51.20
Measured	1.66 ± 0.21	409.34 ± 52.14
% recovery	97	95
Filter Blank	1.51 pM	0.08 nM
Limit of Detection	2.82 pmol kg^{-1}	0.03 nmol kg^{-1}

891

892 **Table 3.** *Properties characterizing the source water types (SWTs[a]) considered in this study. The square of*
893 *correlation coefficients (r^2) between the observed and estimated properties are also given.*

	Potential temperature (°C)	Salinity	O_2^0 (μmol kg^{-1})[b]	NO_3^0 (μmol kg^{-1})[b]	PO_4^0 (μmol kg^{-1})[b]	$Si(OH)_4^0$ (μmol kg^{-1})[b]
UCDW	3.67	34.31	319.00	20.67	1.52	36.51
LCDW	0.40	34.68	345.17	19.99	1.50	115.18
NADW	2.93	34.91	323.28	12.48	0.84	13.21
AABW	-0.47	34.66	353.12	21.92	1.62	124.91
r^2	0.99	0.99	0.97	0.91	0.82	0.93

[a] UCDW: Upper Circumpolar Deep Water; LCDW: Lower Circumpolar Deep Water; NADW: North Atlantic Deep Water; and AABW: Antarctic Bottom Water.

[b] Oxygen (O_2^0), nitrate (NO_3^0), phosphate (PO_4^0) and silicic acid ($Si(OH)_4^0$) represent preformed values; note that O_2 represent saturation.

894

Table 4. *Vertical attenuation factors (b values) for phosphorus (P), particulate zinc (pZn) and particulate cadmium (pCd). ND, no data. The P normalised (P norm) b values for pZn and pCd were obtained by dividing by that of P.*

		all data					< 1000 m				
Lat (°S)	Region	P	pZn	P norm.	pCd	P norm.	P	pZn	P norm.	pCd	P norm.
41	STZ	0.42	0.24	0.57	0.43	1.01	0.40	0.28	0.69	0.40	1.01
43	SAZ	0.56	0.18	0.33	0.52	0.93	0.55	0.23	0.42	0.50	0.92
45	SAZ	0.39	0.24	0.61	0.37	0.96	0.34	0.18	0.53	0.31	0.89
48	PFZ	0.50	0.29	0.57	0.55	1.09	0.49	0.27	0.55	0.52	1.07
50	AAZ	0.45	0.41	0.90	0.50	1.10	0.42	0.39	0.93	0.46	1.08
56	AAZ	0.49	0.37	0.76	0.58	1.18	0.51	0.39	0.76	0.56	1.10
58	AAZ	0.27	0.27	0.97	0.32	1.16	0.23	0.22	0.97	0.27	1.18
All		0.41	0.33	0.78	0.46	1.11	0.39	0.30	0.78	0.43	1.10
Ellwood et al. (2020)	SAZ	2.04	0.82	0.40	2.41	1.18					
Boyd et al. (2017)	South Pacific	0.88 ± 0.48	0.77 ± 0.34	0.88	ND	ND					

List of Figures

936 Figure 1

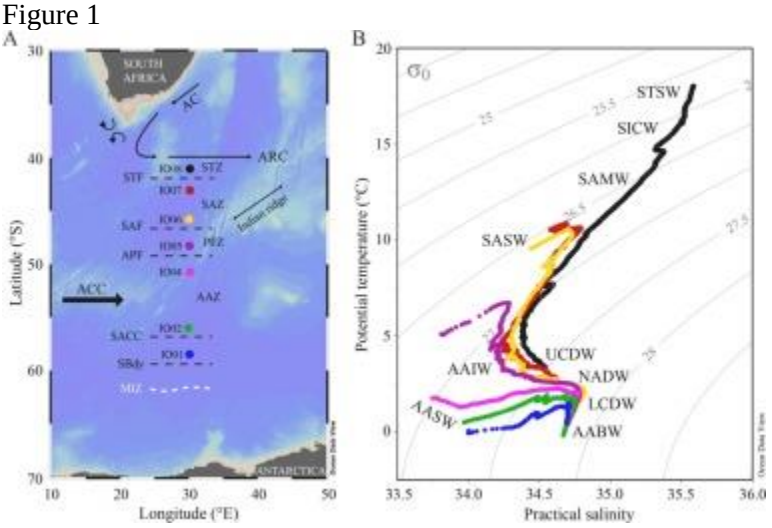

937

938 Figure 2

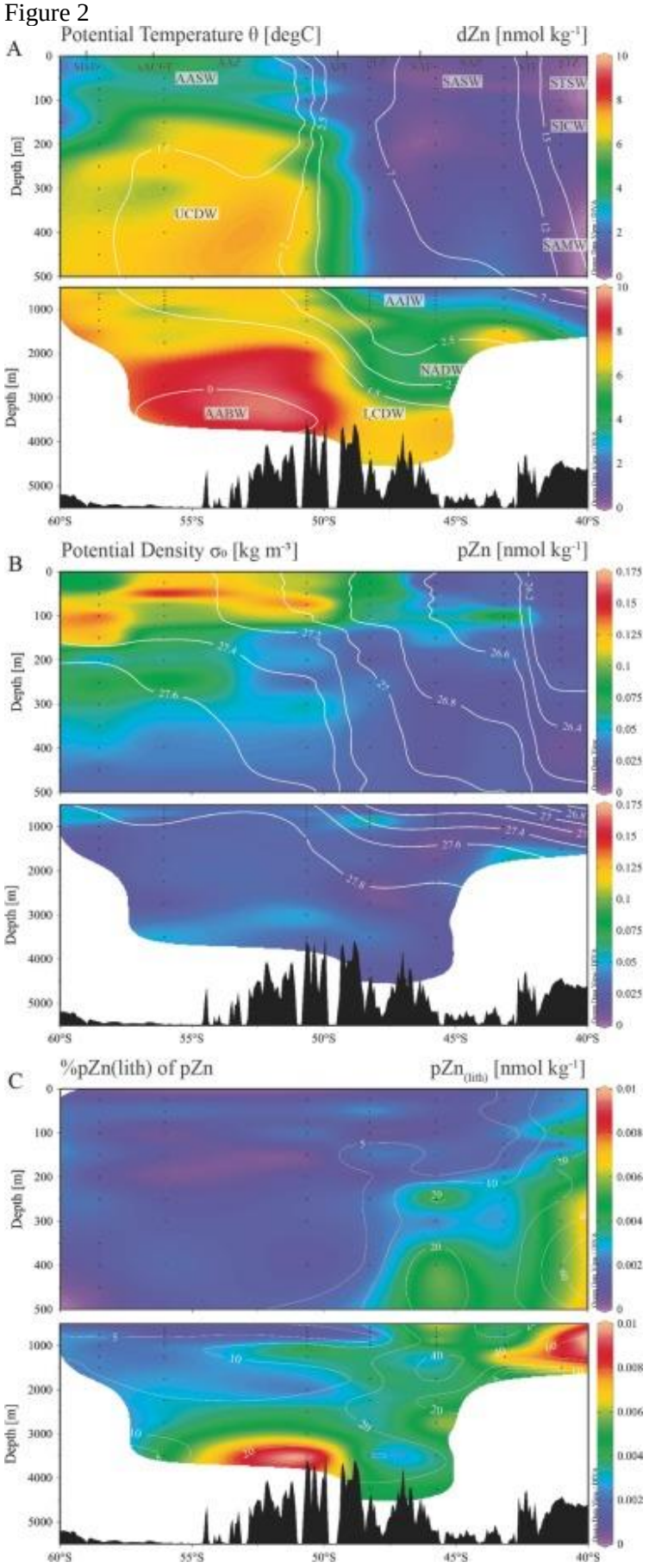

939

940 Figure 3

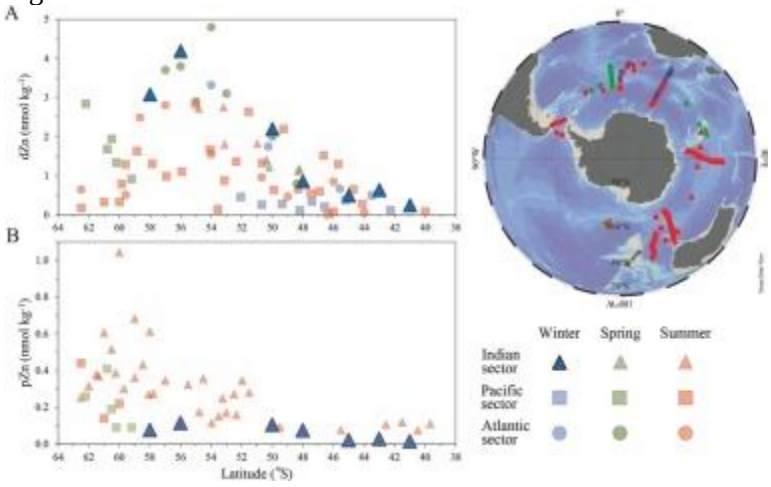

941

942 Figure 4

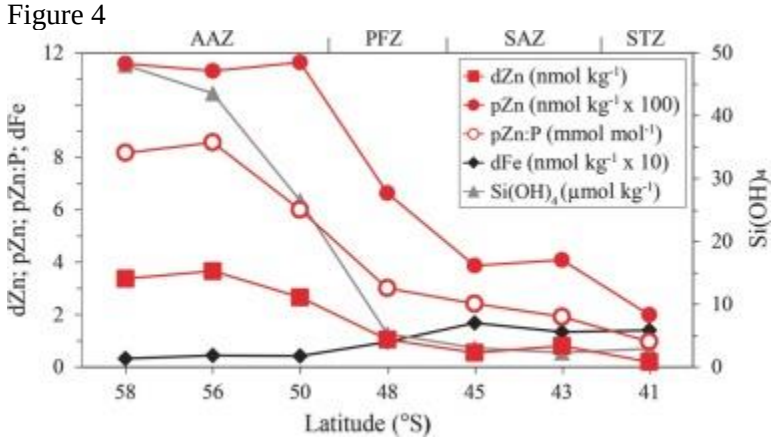

943

944 Figure 5

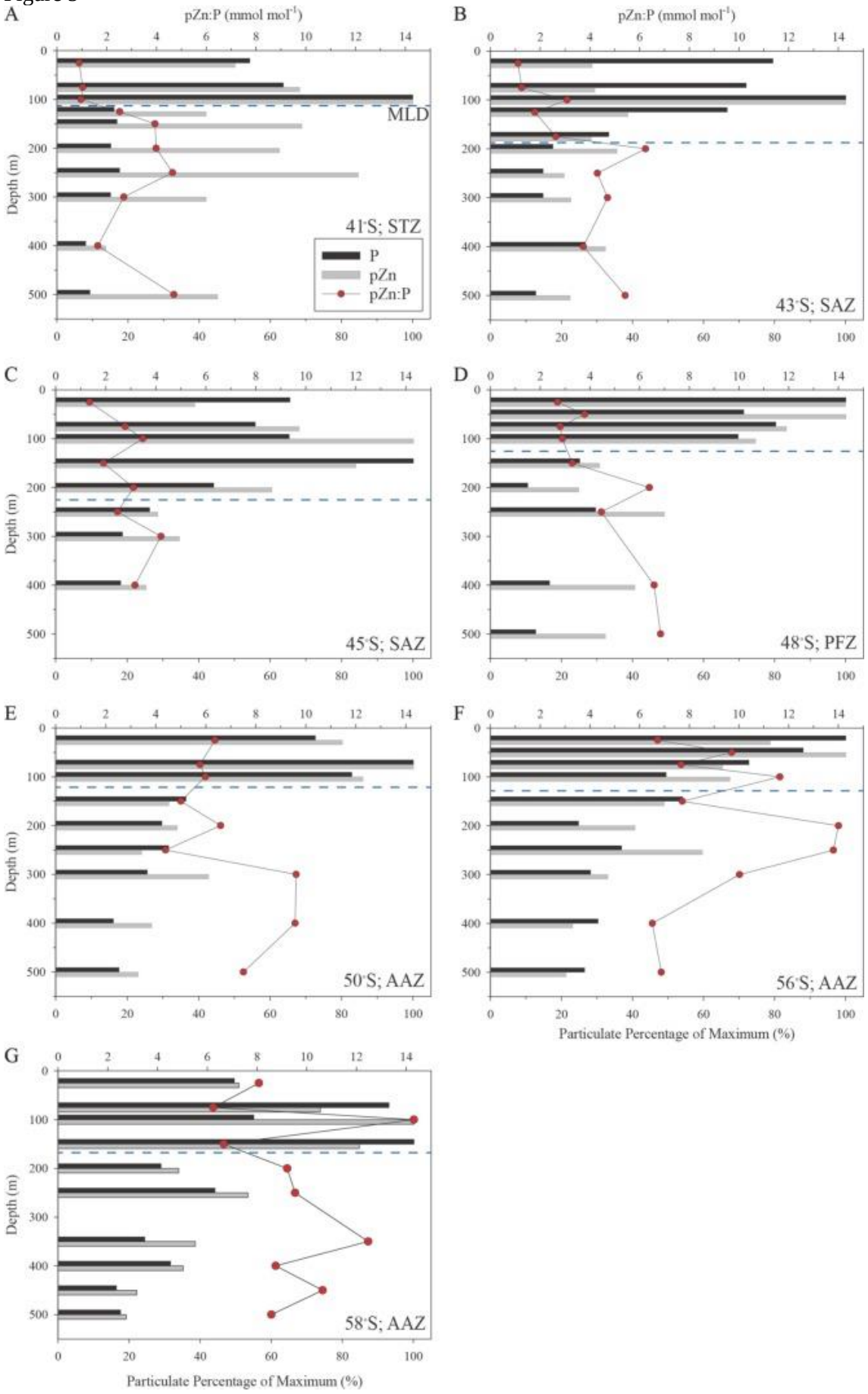

945

946 Figure 6

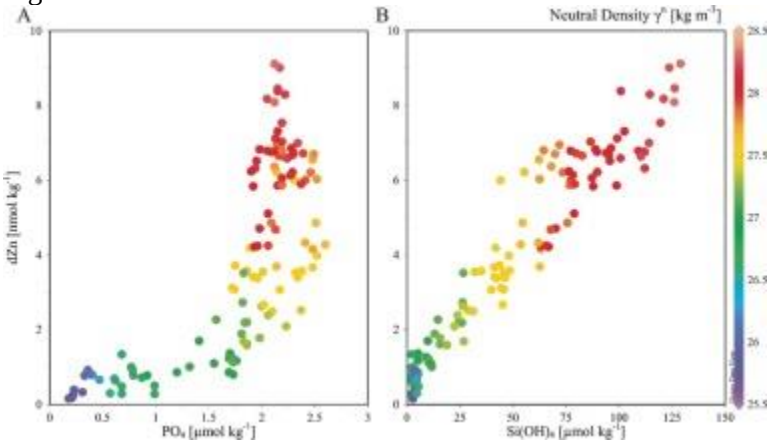

947

948 Figure 7

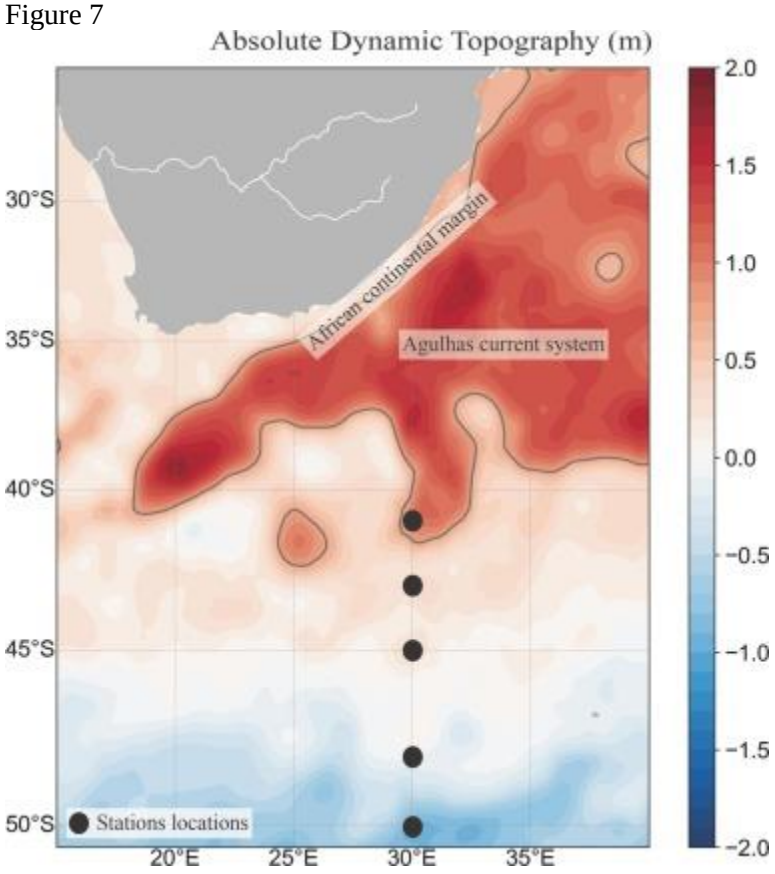

949

950 Figure 8

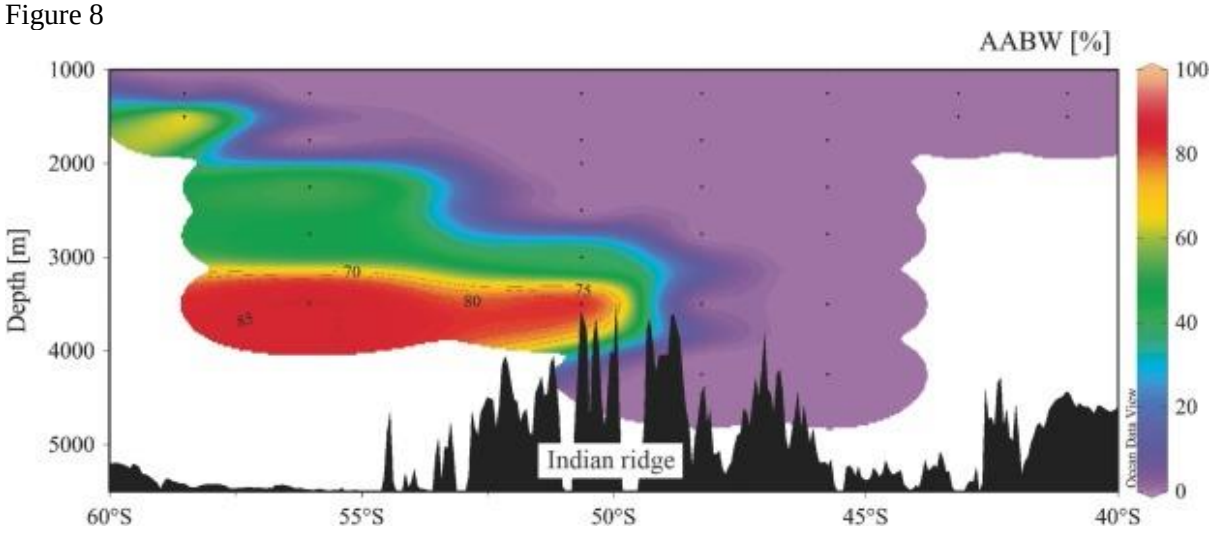

951